creative commons
COMMONS DEED

저작자표시-비영리-변경금지 2.0 대한민국

이용자는 아래의 조건을 따르는 경우에 한하여 자유롭게

- 이 저작물을 복제, 배포, 전송, 전시, 공연 및 방송할 수 있습니다.

다음과 같은 조건을 따라야 합니다:

저작자표시. 귀하는 원저작자를 표시하여야 합니다.

비영리. 귀하는 이 저작물을 영리 목적으로 이용할 수 없습니다.

변경금지. 귀하는 이 저작물을 개작, 변형 또는 가공할 수 없습니다.

- 귀하는, 이 저작물의 재이용이나 배포의 경우, 이 저작물에 적용된 이용허락조건을 명확하게 나타내어야 합니다.
- 저작권자로부터 별도의 허가를 받으면 이러한 조건들은 적용되지 않습니다.

저작권법에 따른 이용자의 권리는 위의 내용에 의하여 영향을 받지 않습니다.

이것은 이용허락규약(Legal Code)을 이해하기 쉽게 요약한 것입니다.

Disclaimer

dCollection

이학박사 학위논문

Electrical Transport in Halogen-doped Graphene

할로겐 도핑된 그래핀의 전하 수송 현상 연구

2012 년 8 월

서울대학교 대학원

물리천문학부

추 승 완

Electrical Transport in Halogen-doped Graphene

할로겐 도핑된 그래핀의 전하 수송 현상 연구

지도 교수 박 영 우

이 논문을 이학박사 학위논문으로 제출함

2012 년 8 월

서울대학교 대학원

물리천문학부

추 승 완

추승완의 이학박사 학위논문을 인준함

2012 년 8 월

위 원 장	국 양	(인)
부위원장	박 영 우	(인)
위 원	유 재 준	(인)
위 원	박 윤	(인)
위 원	김 준 성	(인)

Electrical Transport in Halogen-doped Graphene

Seung Wan Chu

Supervised by

Professor Yung Woo Park

A Dissertation
Submitted to the Faculty of
Seoul National University
in Partial Fulfillment of
the Requirements for the degree of
Doctor of Philosophy

August 2012

Department of Physics and Astronomy
Graduate School
Seoul National University

Abstract

In this dissertation, electrical transport properties of chemically doped graphene with halogen molecules (I_2 and Br_2) are studied. The evidence of doping was also confirmed by Raman spectrum. Here, we expect that the carrier transport in doped graphene gives the chance to investigate the scattering mechanism by dopants.

We have investigated the transport properties of mono and multi-layer graphene doped with halogen molecules, iodine (I_2) and bromine (Br_2). For these doping on monolayer graphene, the charge neutrality point (CNP) shifts to the hole carrier regime indicating p-type doping, and the carrier mobility is reduced. As compared to doping with other dopants, however, the reduction of mobility is much weaker for halogen doping. Halogen molecules can be effective dopants for the graphene monolayer which change the carrier concentration without significant degrading of carrier mobility. This is understood as a reduction of charged impurity scattering by screening due to halogen molecules intercalated between graphene and SiO_2. Also, the maximum resistances (R_{max}) at the CNP are reduced with subsequent doping for the monolayer graphene, in strong contrast to the case with other dopants such as potassium (K), titanium (Ti), platinum (Pt), iron (Fe) and gold (Au). This result is considered as a fingerprint of monolayer graphene in halogen doping. In order to estimate the mobility and R_{max} change, we compare the gate-dependent resistivity to the doping with other dopants. The R_{max} is related with residual carrier density (n_0) due to electron-hole puddle formed by the doping induced impurities on graphene or the charged impurities embedded on SiO_2. The halogen molecules inject charge carriers into electron-hole puddle on graphene. Thus, the residual carrier density induced by doping contributes the conductivity of graphene at CNP. So as to confirm these results, the graphene layer was doped selectively by covering its edge with a

polymer layer. As a result, such unconventional behaviors were not observed any more. Therefore, these observations can be understood that intercalated halogen molecules between the graphene layer and the underlying substrate leads to screening of the charged impurities embedded in SiO_2 substrate.

The hole doping effect by halogen molecules was measured in multi-layer graphene and CNP shift was observed, too. However, on the contrary to the result of monolayer graphene, the R_{max} increasing with doping was observed. Because halogen molecules can be intercalated into graphene layers and underlying graphene, screening effect is considered to be weakened. However, unfortunately, the origin of this effect was not interpreted clearly. In order to understand the effect, further qualitative and quantitative descriptions are needed.

The evidence of doping can be observed Raman spectrum as well as electrical transport measurement. Although there are several previous data of Raman spectrum for doped graphene, we can obtain the information of halogen doping on graphene. There are two main effects of halogen doping which are well known on other types of doping. One is the G-peak upshift which is observed in I_2- and Br_2-doped monolayer graphene. In particular, G-peak splitting was observed in multi-layer graphene doped with Br_2 on account of intercalation between graphene layers. The other is reduction of 2D-peak intensity. It is interpreted as an electron-electron scattering effect. Additionally, the stability of halogen doping was estimated with the observation of G-band shifts by aging. After 2 months later, the G-peak downshifts were observed. However, as the number of layer increases, the shifts are small or negligible.

The electrical transport measurement was performed in a high vacuum in order to minimize the oxidation of electrodes during detection of electrical signal. And the halogen doping was performed in a glass tube that is inert on halogen molecules at room temperature.

Keywords : Graphene, Halogen Doping, Electrical Transport, Charged Impurity scattering, Doping induced-impurity scattering, Raman Spectrum

Student ID Number : 2002-30142

Contents

1. Introduction 1

1.1 Graphene Doping 1
1.2 Scattering in Graphene 4
1.3 Resistance with carrier density in Graphene 13
1.4 Raman Spectrum of Graphene 13
1.5 Outline of Thesis 19

2. Experimental 24

2.1 Graphene Extraction and Device Fabrication 24
2.2 Halogen Doping 26
2.3 Electrical Measurement 28
2.4 Raman Spectroscopy 28

3. Electrical Properties of Halogen-doped Mono and Multi-layer graphene 30

3.1 Results and Discussion 30
3.2 Summary 48

4. Characterization by Raman Spectrum and AFM of Haolgen-doped Graphene 51

4.1 Results and Discussion 51
4.2 Summary 56

5. Conclusion 59

List of Figures

1.1 (a) Lattice structure of a mono (left) and bi-layer (right) graphene. (b) Energy band of monolayer graphene. The conduction band and the valence band are connected at one point (K or K'). 2

1.2 (a) Gate voltage-dependent conductivity of K-doped monolayer graphene. (b) Gate voltage dependence of NO_2-doped monolayer graphene (left). In-situ resistances of NH_3, CO, NO_2 and H_2O-doped monolayer graphene are displayed. 2

1.3 (a) Dielectric screening in graphene. (b) Gate-dependent conductivity for Ne^+ ion-irradiated graphene. 3

1.4 (a) Ionic liquid-doped monolayer graphene. (b) Monolayer graphene doped with protein molecules of various pH values. 3

1.5 Charged impurities between graphene layer and SiO_2. 4

1.6 (a) Wave vector scheme of monolayer graphene in *k*-space. (b) Projection of waver vector scheme of (a). 6

1.7 (a) Reduction of charged impurity scattering by dielectric screening. (b) Enhancement of electron-electron scattering due to dielectric medium surrounded the charge carriers. 8

1.8 (a) Raman spectrum of pristine and ion (Ne^+)-irradiated graphene. (b) Gate-dependent conductivity of Ne^+-irradiated graphene. 10

1.9 Temperature-dependent resistivity of graphene on SiO_2 and the fitting lines. 12

1.10 (a) Schematics of Raman spectroscopy. (b) Raman spectrum of monolayer graphene. 14

1.11 A Schematic diagram of G-band transition in Raman spectrum. 15

1.12 A Schematic diagram of D-band in Raman spectrum. 15

1.13 (a) A Schematic diagram of 2D-peak in Raman spectrum. (b) Electron-hole pair creation and recombination in two phonon scattering.....16

1.14 DR process and transition energy levels in trigonal warping system. 17

1.15 Electron energy band (below) and phonon dispersion (above) with phonon density of states of a monolayer graphene. 17

1.16 (a) Phonon dispersion of graphene. Kohn anomaly is indicated at K- and Γ-points. (b) Electron band in the presence of lattice distortion which causes non -adiabatic deformation of electron system. 18

1.17 (a) G-band width variation with Fermi-level shift. (b) Allowed phonon decay into electron-hole pair. (c) Phonon decay into electron-hole pair is forbidden by Pauli exclusion principle. 18

2.1 (a) A part of mask pattern in pre-patterned Si/SiO_2 substrate. (b) The exfoliated graphene layers are on the Si/SiO_2 substrate. 25

2.2 Raman spectrum of pristine monolayer graphene. Inset shows a single peak fitting with Lorentzian of 2D-peak. 25

2.3 (a) A graphene device fabricated by standard e-beam lithography on Si/SiO_2 substrate. (b) A magnification of a fabricated device in figure (a). 26

2.4 Purification of halogen molecules before doping by evacuation with a sequence of freezing and thawing. 27

2.5 (a) A picture of doping setup. Halogen doping is confirmed with glass doping line. (b) The samples are mounted under the chip connector. 27

2.6 A schematic diagram of halogen doping setup. 28

3.1 An AFM image of a graphene device and a measurement scheme.. 30

3.2 Dirac voltage (V_D) shifts with respect to evacuation time after I_2 doping at each doping level. 31

3.3 In-situ resistance of Br_2-doped monolayer graphene at Vg=0 V. 32

3.4 The gate-dependent resistances of I_2-doped monolayer graphene at room temperature in a high vacuum (~10^{-5} Torr). 33

3.5 The data of forward sweep direction in Fig. 3.4. 33

3.6 A Schematic diagram of I_2-doped graphene device (left). I_2 adsorbed on graphene is formed the iodine anion, I_3^- and I_5^-, which gives holes to carbon atoms (right). 35

3.7 The Fermi-level modulation by doping. 35

3.8 (a) Hysteresis of gate-dependent resistance of monolayer graphene. (b) It is caused by capacitive charging effect such as avalanche injection from graphene to SiO_2 dielectric layer by applied gate voltage.....36

3.9 The gate-dependent resistance of Br_2-doped monolayer graphene at room temperature. 37

3.10 High symmetry adsorption for Br_2 molecules on graphene. (a)~(c) are perpendicular and (d)~(f) are parallel adsorption to graphene sheet. 37

3.11 Electron and hole mobility values of doping by various dopants with respect to Dirac voltage shift (V_D-V_0). 39

3.12 The normalized mobility (μ/μ_0) of doping by various dopants with respect to Dirac voltage shift (V_D-V_0). 40

3.13 The normalized average mobility ($<\mu>/<\mu_0>$) of doping by various dopants with respect to Dirac voltage shift (V_D-V_0). 40

3.14 Dirac voltage shift (V_D-V_0) vs. $1/\mu$-$1/\mu_0$ of halogen doping with the data from doping with various dopants. 41

3.15 The normalized maximum resistance ($R_{max}/R_{max,0}$) of monolayer graphene doped with various dopants, where $R_{max,0}$ is R_{max} of undoped graphene.. 41

3.16 Charge distribution on graphene by inhomogeneous potential fluctuation due to the charged impurities embedded on SiO_2 42

3.17 The gate-dependent resistance of I_2-doped monolayer graphene with its edge covered by PMMA. 44

3.18 The normalized resistance ($R_{max}/R_{max,0}$) of I_2-doped monolayer graphene. 44

3.19 Temperature-dependent 4-probe resistivity of I_2-doped monolayer graphene. 45

3.20 The gate-dependent resistances of halogen-doped multi-layer graphene. ..46

3.21 Gate-dependent resistance of Br_2-doped monolayer graphene with its edge covered by PMMA. 47

3.22 (a) Current flow as a function of evacuation time with various gate voltages in bi-layer graphene. (b) dI_{ds}/dV_g vs. evacuation time in bi-layer graphene. 47

4.1 Raman spectrum of I_2- and Br_2-doped monolayer graphene. 52

4.2 Optical microscope image of graphene layers doped with Br_2 (1 min) on SiO_2 thickness of 300 nm. 53

4.3 Raman spectrum of Br_2-doped graphene layers. (a), (b), (c) and (d) are the results of layer 1, 2, 3 and 4 in Fig. 4.2. 53

4.4 Raman spectrum of aged (2 months) graphene after Br_2 doping. (a), (b), (c) and (d) are spectrums of layer 1, 2, 3 and 4 in Fig. 4.2. 54

4.5 (a) An AFM image of undoped graphene. (b) The profile (height=1.6 nm) of undoped graphene. (c) An AFM image of I_2-doped graphene. (d) The height information (2.7 nm) of I_2-doped graphene. 55

4.6 AFM images of a monolayer graphene device. (a) Height information and (b) voltage information of undoped graphene device. (c) Height information and (d) voltage information of I_2-doped graphene device. 55

4.7 AFM images of a monolayer graphene device. (a) Height information and (b) voltage information of undoped graphene device. (c) Height information and (d) voltage information of Br_2-doped graphene device.. 56

List of Tables

3.1 Binding energy, bond length (Br-Br) and the distance between Br_2 and graphene 38

Chapter 1

Introduction

Before we show the experiment and result directly, it will help for us to introduce the background understanding for graphene doping with charge transport and Raman spectrum analysis. So, we briefly exhibit the basic description about scattering in graphene and information of lattice vibration.

1.1 Graphene doping

Graphene is two dimensional one atomic layer of hexagonal carbon structure with linear electron energy dispersion. There are two carbon atoms in unit cell of monolayer graphene with the lattice constant of a=2.46 Å (Fig. 1.1(a)). Since 2004, because of its exotic properties and possibilities for applications, several experimental and theoretical studies have been performed. However, because of the absence of band gap in graphene, the applications for semiconducting electronic device are highly limited.

Although graphene has no band gap, it is valuable to use other good properties. In particular, the conductivity and the mobility are the most important properties as a performance of electronic devices. In order to introduce additional functionalities in graphene and to develop the graphene-based electronic applications, however, the control of the electronic properties of graphene such as gap opening, *n*- and *p*-type doping is crucial, and thus the modification of the electronic properties of graphene has been tried with various chemical doping.

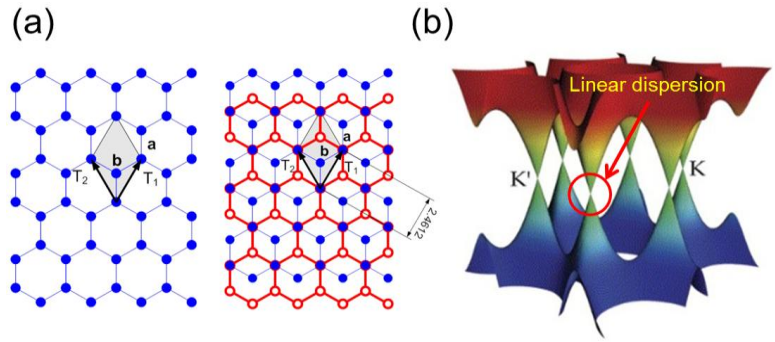

Figure 1.1. (a) Lattice structure of a mono (left) and bi-layer (right) graphene. (b) Energy band of monolayer graphene. The conduction band and the valence band are connected at one point (K or K') [1].

There are several experimental results of graphene doping with various dopants such as K, Ti, Pt, Fe, Au, gas molecules, liquid dielectric materials and so on. For K doping on monolayer graphene [2], the CNP is shifted to electron carrier regime. The mobility reduction is interpreted with the scattering by the charged impurities embedded on SiO_2 dielectric layer (Fig. 1.2 (a)) [2]. The doping with various gas molecules are represented in Fig. 1.2(b) [3]. Here, NH_3 and CO are *n*-type and NO_2 and H_2O are *p*-type dopants. In contrast to K doping, the mobility reduction is not significant. The enhanced graphene mobility was obtained with the dielectric screening by using ice layers which limits the Coulomb interaction between charge carriers and the charged impurities (Fig. 1.3(a)) [4]. Not only long range scattering but

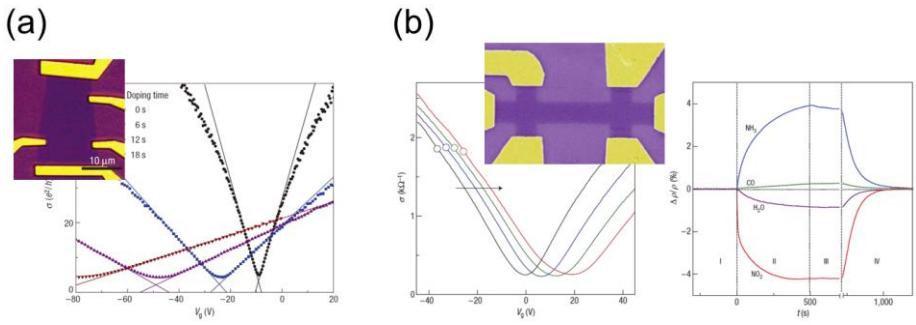

Figure 1.2. (a) Gate voltage-dependent conductivity of K-doped monolayer graphene [2]. (b) Gate voltage dependence of NO_2-doped monolayer graphene (left). In-situ resistances of NH_3, CO, NO_2 and H_2O-doped monolayer graphene are displayed [3].

also short range scattering by defect due to charged ions (He^+, Ne^+) are studied (Fig. 1.3(b) [5].

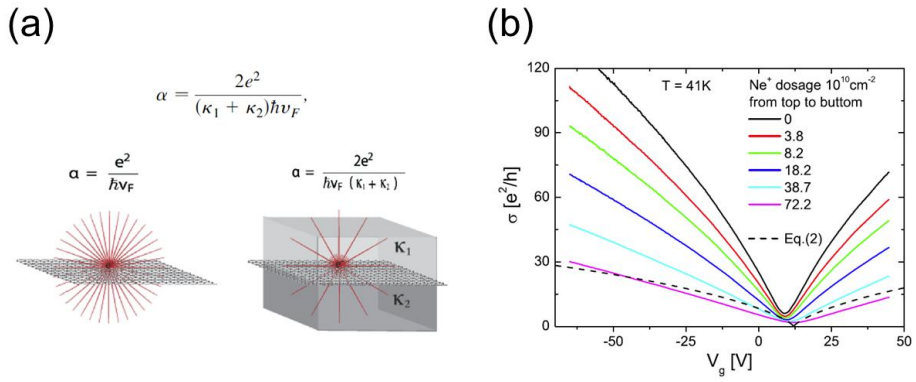

Figure 1.3. (a) Dielectric screening in graphene [4]. (b) Gate-dependent conductivity for Ne^+ ion-irradiated graphene [5].

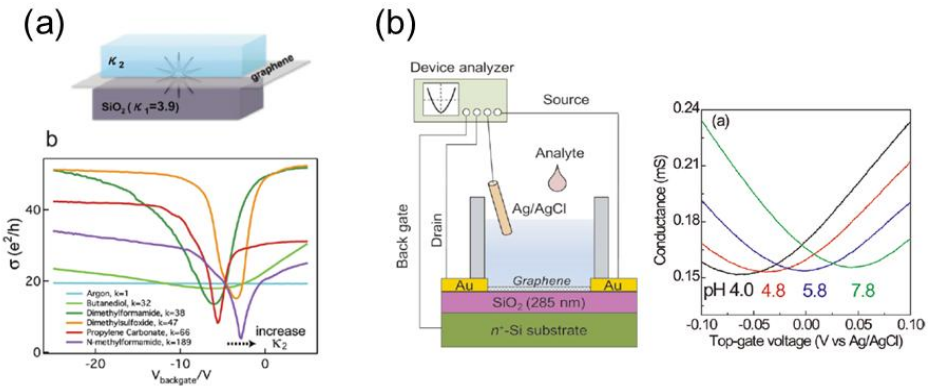

Figure 1.4. (a) Ionic liquid-doped monolayer graphene [6]. (b) Monolayer graphene doped with protein molecules with various pH values [7].

Moreover, liquid phase doping have attracted attention because of the potential for enormous charge accumulation and the dielectric screening (Fig 1.4 (a)) [6]. The ionic liquid plays a role of ionic screening dielectric layer also. In figure 1.4 (b), the graphene is doped with protein molecules of various pH values [7].

Even though, there are already a lot of studies of graphene doping as mentioned above, halogen molecules are of interest. Because a dramatic increasing of conductivity with hole doping is expected in contrast to various *n*-type doping with other dopants such as K, Ti, Fe, Pt and Au [2, 8, 9], the studies on mobility and conductivity are valuable to application for conducing device. Recently, several experimental and theoretical results of halogen-doped graphitic materials have been reported. Adsorption and intercalation mechanism of halogen molecules were calculated by density functional theory [10, 11]. Charge transfer and band gap formation by iodine (I_2) and bromine (Br_2) doping in few-layer graphene were observed with Raman spectroscopy [12]. I_2-doped graphene film was synthesized by a mixture of I_2 and camphor with CVD [13]. Supermetallic conductivity and optical property were observed in Br_2 intercalated HOPG [14]. So far, however, there has been no experimental study on the charge transport properties of graphene doped with halogen molecules near Dirac point.

1.2 Scattering in graphene

1.2.1 Linear conductivity by long range Coulomb scattering

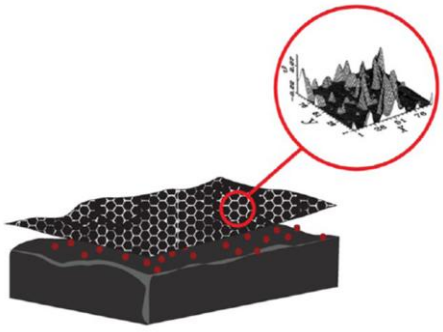

Figure 1.5. Charged impurities between graphene layer and SiO_2 [15].

In a high mobility graphene, ballistic transport regime, the conductivity exhibits the sub-linear dependence at high gate voltage region. However, if the graphene has low mobility due to scattering by the impurity or defect, the conductivity follows a linear dependence of gate voltage at $V \neq V_{CNP}$, where V_{CNP} is a voltage at charge neutrality point. The linear dependence of conductivity is mostly shown in doped graphene (Fig. 1.2(a)). At low mobility and high carrier density regime, the Boltzmann transport theory is an appropriate approach for description of semi-classical scattering mechanism. The conductivity of an electron system is obtained by the Boltzmann transport formalism as

$$\sigma = \frac{e^2}{2}\int d\varepsilon D(\varepsilon) v_k{}^2 \tau(\varepsilon)\left(-\frac{\partial f(\varepsilon)}{\partial \varepsilon}\right), \tag{1.1}$$

where, v_k and $\tau(\varepsilon)$ are carrier velocity and momentum relaxation time. In graphene, density of states is known as

$$D(\varepsilon) = \frac{2\varepsilon}{\pi \hbar^2 v_F{}^2}, \tag{1.2}$$

where, v_F (=1.1 x 10^6 m/s) is Fermi velocity of graphene. Note that Boltzmann distribution function of electron is written as

$$f(\varepsilon) = \frac{1}{1+\exp(\frac{\varepsilon - E_F}{k_B T})} \quad \text{and at } T=0, \quad f(\varepsilon) = \Theta(-\varepsilon + E_F). \tag{1.3}$$

Thus the conductivity is represented as

$$\sigma = \frac{e^2 v_F{}^2}{2} D(\varepsilon)\tau, \tag{1.4}$$

and the scattering of charge carriers are allowed by Fermi's golden rule as

$$\frac{1}{\tau} \sim \frac{2\pi}{\hbar} \left| \langle k_f | V | k_i \rangle \right|^2 D(\varepsilon) . \tag{1.5}$$

Because the relaxation time depends on electric potential *V*, conductivity is also affected by the shape of the potential. Long range scattering is a Coulomb scattering by the charged impurity which is the most important scattering mechanism in graphene [15] (Fig. 1.5). The Coulomb potential is written as

$$V = \frac{2\pi e^2}{\kappa k} , \tag{1.6}$$

where κ and k are dielectric constant and electron wave vector (Fig. 1.6).

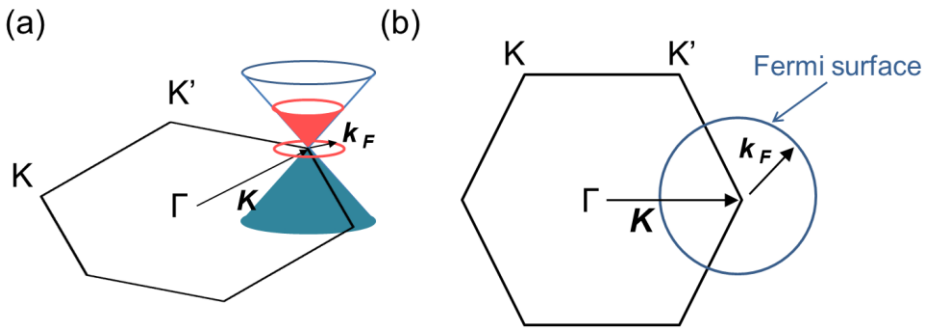

Figure 1.6. (a) Wave vector scheme of monolayer graphene in *k*-space. (b) Projection of waver vector scheme of (a).

Although the interaction between charge carriers and the charged impurities is *k*-dependent, scattering events occur near Fermi-level mostly.

$$k \sim k_F$$

And in graphene, the eigen states are obtained as

$$|k\rangle = \frac{1}{\sqrt{2}} e^{i\vec{k}\cdot\vec{r}} \begin{pmatrix} ie^{-i\frac{\theta_k}{2}} \\ \pm e^{i\frac{\theta_k}{2}} \end{pmatrix}, \tag{1.7}$$

thus,

$$\left|\langle k_f | V | k_i \rangle\right|^2 = \left(\frac{1}{\kappa k_F}\right)^2, \tag{1.8}$$

where, $\pm$ corresponds to electron and hole band and $\theta_k = \tan^{-1}\left(\frac{k_x}{k_y}\right)$.

Therefore, the conductivity in the presence of randomly distributed charged impurities shows linear behavior with carrier density which is proportional to carrier density as

$$\sigma_L \sim \kappa^2 {k_F}^2 \sim n \sim V_g . \tag{1.9}$$

1.2.2 Constant conductivity by short range scattering (weak point disorder)

The phonons and point defects that are weak point disorders play a role of short range scatterers which shows the different behavior with long range Coulomb scattering. Because the short range potential is independent on carrier density, the momentum relaxation time and density of states have the relation as below,

$$\frac{1}{\tau D(E)} \sim \frac{2\pi}{\hbar}\left|\langle k_f | V | k_i \rangle\right|^2 = Const. \tag{1.10}$$

thus,

$$\sigma = \frac{e^2 v_F{}^2}{2} D(E)\tau = Const. \qquad (1.11)$$

This implies the Fermi energy-independent conductivity of short range scattering with weak point disorder or impurity. The weak interaction of these scatterers is not intervalley scattering which can cause the back scattering. It is distinguished from the scattering with lattice defect.

1.2.3 Dielectric screening

Charge transport of graphene in dielectric medium shows distinguished behaviors from the results by another scattering. There are three main screening effects of the dielectric material, that is, carrier mobility (μ_L) increasing, enhancement of conductivity (σ_s) due to short range scattering and constant minimum conductivity (σ_{min}). The opposite behaviors of μ_L and σ_s were explored by an addition of dielectric ice layer on graphene [5].

First, the carrier mobility (μ_L) is enhanced by the dielectric screening. If the graphene is surrounded by dielectric medium, the long range Coulomb potential due to the charged impurities embedded on SiO_2 is normalized by dielectric screening. Thus, the carrier mobility is increased as a result of the reduction of charged impurity scattering due to dielectric screening (Fig. 1.7(a)).

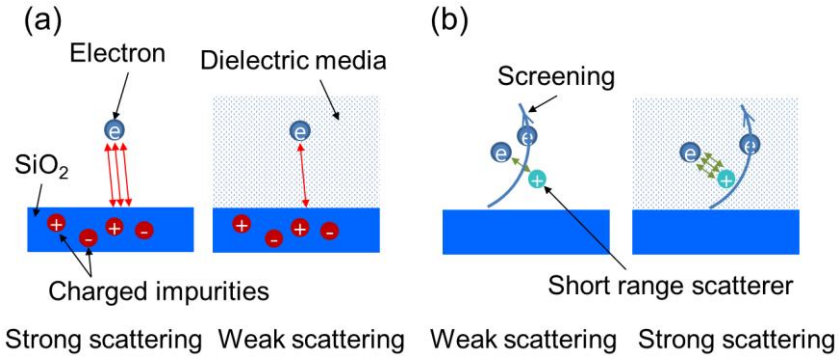

Figure 1.7. (a) Reduction of charged impurity scattering by dielectric screening. (b) Enhancement of electron-electron scattering due to dielectric medium surrounded the charge carriers.

Second, the conductivity due to short range scattering (σ_s) is decreased due to reduction of electron-electron screening. The electrons in graphene interact with other electrons with their interaction strength α, a ratio between Coulomb potential energy and kinetic energy. If the electron wavelength is $\lambda=2\pi a$, α can be represented as

$$\alpha = \frac{E_{Coulomb}}{E_{Kinetic}} = \frac{e^2 / 4\pi\varepsilon a}{\hbar v_F k} = \frac{e^2 / 4\pi\varepsilon a}{\hbar v_F / a} = \frac{e^2}{4\pi\varepsilon\hbar v_F}, \qquad (1.12)$$

where, a is a distance between two electrons. α is a dimensionless electron-electron coupling constant and describes the relative strength of Coulomb interaction. It is independent on electron density and also known as fine structure constant in graphene with the analogy of $c \rightarrow v_F$ and $\varepsilon_0 \rightarrow \varepsilon$. In pristine graphene, the short range scattering between electrons and scatterers is screened by electron population. However, if the electrons are surrounded by dielectric medium, electron-electron coupling is decreased. It is quantitatively explained with the increasing of ε (= $\kappa\varepsilon_0$) in eq. 1.12. As a result, the σ_s is limited by the stronger short range scattering (Fig. 1.7(b)).

Third, the minimum conductivity (σ_{min}) is unchanged because of the compensation between electron-hole puddle density and mobility. In the environment of dielectric screening, the interaction between the charged impurities embedded on SiO_2 and graphene sheet is weakened. This is a cause of mobility enhancement and the decreasing of electron-hole puddle density. Owing to the inhomogeneous potential fluctuation, electron-hole puddle is formed. However, because of dielectric screening, the bumpy surface of graphene becomes rather flat. As a result, the carrier density due to electron-hole puddle is decreased.

1.2.4 Lattice defect scattering

Defect induced scattering has been studied by the doping with ions which forms the atomic defects. Ion irraidation effect in graphene was reported with the conductivity and mobility studies [6]. The ionic dopants, He^+ and Ne^+, are induced on graphene with irradiation energy of 500eV. The defect formation in graphene is identified with the presence of D-peak in Raman spectrum (Fig.

1.8(a)). From the result of ionic irradiation, we can catch the important information of defect scattering.

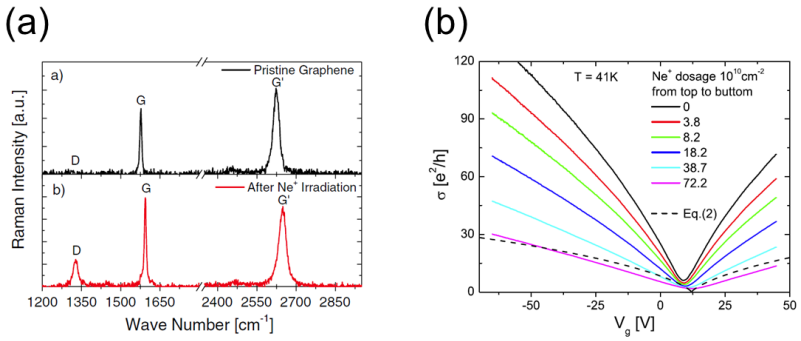

Figure 1.8. (a) Raman spectrum of pristine and ion (Ne^+)-irradiated graphene. (b) Gate-dependent conductivity of Ne^+-irradiated graphene [6].

First, CNP shift is small or negligible with doping. It is a difference from the doping of affected by charged impurity scattering. Moreover, the direction of CNP shift is opposite to the expectation.

Second, mobility decreases with irradiation because of defect scattering. Even though this result looks like similar with the behavior of other scattering, it is distinguished because of 4 times smaller mobility with same carrier concentration.

Third, conductivity decreases proportional to mobility decreasing (Fig. 1.8(b)). It is another indisputable difference with charged impurity scattering which also shows the conductivity reduction at CNP. In Drude model, conductivity is written as

$$\sigma = \mu n e . \tag{1.13}$$

This is also valid at CNP as

$$\sigma_{\min} = \mu n_0 e . \tag{1.14}$$

In graphene affected by charged impurity scattering, σ_{min} increases with doping because of the residual carrier density (n_0) increasing. However, in graphene influenced by defect scattering, the n_0 do not increases, and σ_{min} decreases slightly proportional to mobility reduction.

Although defect is also short range scattering source, it shows different behaviors from the scattering by weak disorder and impurity. The conductivity of scattered graphene with defect is known to be followed the midgap state model. The defect roughly considered as a strong deep potential with the radius *R*, and the conductivity is described as

$$\sigma_d = \mu ne = \frac{2e^2}{\pi h}\frac{n}{n_d}\ln^2(k_F R), \tag{1.15}$$

where, n_d is the defect density.

At low temperature, conductivity reduction was observed with the temperature decreasing. This is interpreted as a possibility of metal-insulator transition at low temperature in defect formed graphene.

1.2.5 Scattering with optical phonon in substrate (a remote interfacial phonon)

Graphene resistivity due to electron-acoustic phonon scattering is known as about 30 Ω which shows linear increasing with temperature (eq. 1.16) and independent on electron density. However, the resistivity of graphene on SiO_2 substrate shows the drastic increasing at T>200 K (Fig. 1.9(a)) [16]. This cannot be explained with acoustic phonon scattering in graphene, thus the effect by substrate was considered as an extrinsic scattering source. J. –H. Chen *et al*. investigated the thermally activated contribution to resistivity with the model of surface phonons in SiO_2 as

$$\rho = \rho_0(V_g) + \rho_A(T) + \rho_B(V_g, T)$$

with

$$\rho_A(T) = (\frac{h}{e^2}) \frac{\pi^2 D_A{}^2 k_B T}{2h^2 \rho_s v_s{}^2 v_F{}^2} \tag{1.16}$$

and

$$\rho_B(V_g, T) = BV_g{}^{-\alpha} (\frac{1}{e^{(59meV)/k_B T} - 1} + \frac{6.5}{e^{(155meV)/k_B T} - 1}), \tag{1.17}$$

where, $\rho_0(V_g)$, $\rho_A(T)$, $\rho_B(T,V_g)$, D_A, ρ_s and v_s are the residual resistivity at low temperature, the resistivity due to acoustic phonon scattering, the resistivity due to scattering by optical phonon in SiO_2, acoustic deformation potential, mass density of graphene and sound velocity, respectively [16]. Here, α (=1.04) is consistent with the value of 1, which is exponent of gate voltage with respect to carrier density. It is well known that the energies of the two strongest optical phonon modes are 59 and 155 meV. Therefore, the exponents of Bose-Einstein distribution term in eq. 1.17 are represented with the values. Fig. 1.9(b) shows the electron scattering with an optical phonon in SiO_2 and an acoustic phonon in graphene.

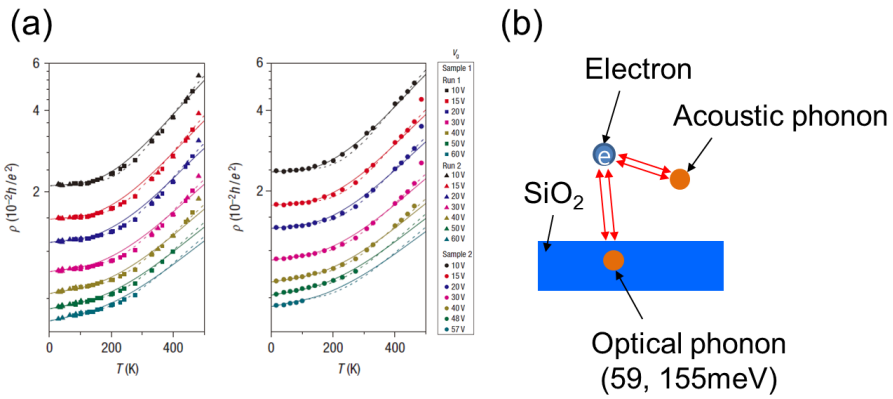

Figure 1.9. Temperature-dependent resistivity of graphene on SiO_2 and the fitting lines [16].

1.3 Resistance with carrier density in graphene

Gate-dependent resistance of graphene can be fitted with

$$R = \frac{(L/W)}{e\mu\sqrt{n^2 + n_0^{\ 2}}} = \frac{(L/W)}{e\mu\sqrt{\alpha^2(V_g - V_0)^2 + n_0^{\ 2}}}, \qquad (1.18)$$

where, L, W, μ and n_0 are channel length, channel width, carrier mobility and doping induced residual carrier density [17]. The mobility and doping induced residual carrier density in 4-probe gate-dependent resistance were obtained from the above equation. α (7.2×10^{10} $V^{-1}cm^{-2}$) is a proportional constant related with gate-induced carrier density as $n=\alpha V_g$, and decided by the geometry of SiO_2 dielectric capacitor thickness of 300 nm as

$$n = \frac{c_g}{e}V_g = \left(\frac{\varepsilon\varepsilon_0}{et}\right)V_g, \qquad (1.19)$$

where, c_g (1.15×10^{-4} F/m^2) and t are capacitance per unit area and thickness of SiO_2.

1.4 Raman spectrum of graphene

Raman spectroscopy is a non-destructive characterization technique for investigation of lattice vibration information. And, it is one of the important tools for carbon based materials. In particular, Raman spectrum of graphene is a direct identification of the number of layers, defect, doping and intercalation. So, we introduce the meaning of the Raman bands of graphene briefly.

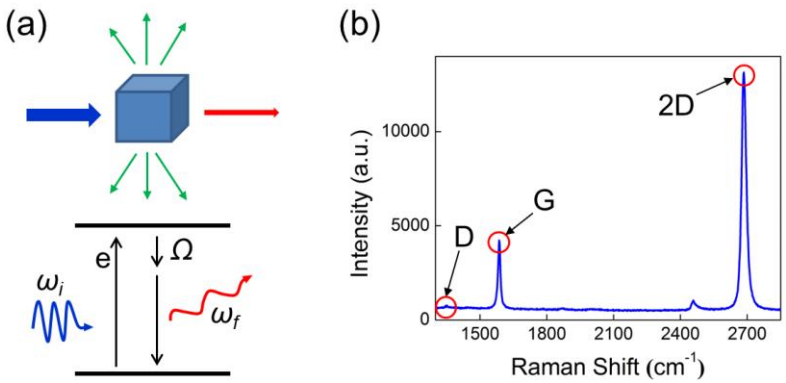

Figure 1.10. (a) Schematics of Raman spectroscopy. (b) Raman spectrum of monolayer graphene.

The concept of Raman spectrum is demonstrated in Fig. 1.10(a) with the transition of lattice vibration. The excited electrons are scattered by phonon with the momentum and energy exchanges. Then, we detect the energy difference between incident and irradiated photons, namely Raman shift. There are three outstanding peaks (G, D and 2D-peak) in Raman spectrum of graphene (Fig. 1.10(b)). These peaks indicate the lattice vibration in each phonon state of graphene.

1.4.1 G-peak

G-peak of Raman spectrum in graphene is associated with scattering by phonons in Γ-band [18]. In Fig. 1.11, the transition is represented with the lattice vibration, E_{2g} mode, indicating the asymmetry atomic vibration in hexagonal lattice. In this process, phonon takes the energy of ω_G from the excited electron. However, the momentum exchange is negligible (**q**≈0).

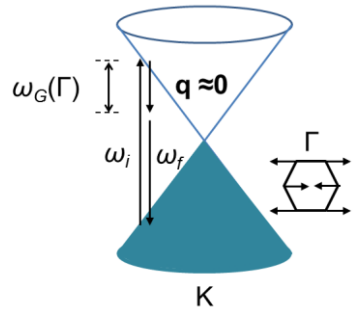

Figure 1.11. A Schematic diagram of G-band transition in Raman spectrum [18].

1.4.2 D-peak

D-peak of Raman spectrum in graphene is concerned with the electron scattering by the K-band phonon [19]. In Fig. 1.12, the transition is represented with the lattice vibration (a breathing mode of A_1' symmetry). The excited electron exchanges the momentum '**q**' with a phonon (electron-hole pair creation) and returns to K-point after scattering with defect. Then, finally, the electron-hole recombination is occurred. In this process, the excited electron loses the energy ω_D during the scattering with phonon. However, in transition of reverse direction, there is no energy exchange because of the elastic scattering with defect.

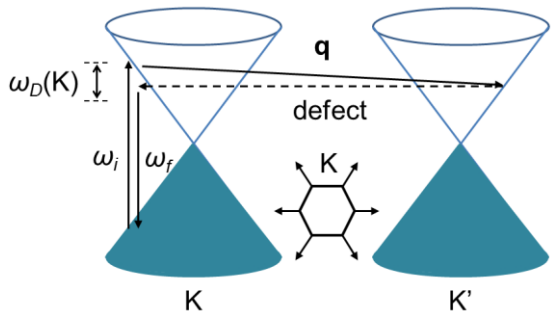

Figure 1.12. A Schematic diagram of D-band transition in Raman spectrum [19].

1.4.3 2D-peak

2D-peak is considered as the most distinguishable character on identification of number of layers in graphene. Usually, the intensity ratio between 2D- and G-peak [I(2D)/I(G)] of monolayer graphene is 2~3. As increase the number of layers, I(2D)/I(G) decreases. FWHM (Full Width Half Maximum) of 2D-peak, can be fitted with Lorentzian peaks, also indicates the number of layers. In case of mono and bi-layer graphene, FWHM is ~30cm^{-1} and 50cm^{-1}, respectively. Fig. 1.13(a) and (b) show the Raman scattering process of 2D-peak in graphene. The difference from the transition of D-peak is the scattering with second phonon. In this returning process, an electron is scattered (inelastic scattering) by a phonon with an opposite momentum '**-q**', thus the energy loss is double what occurs in D-peak transition. It makes an overtone of D-peak in Raman spectrum. This process is known as double resonant (DR) scattering [20].

Fig. 1.14 shows a top view of DR scattering event in first Brillouin zone. Because of trigonal warping, the electron energy level is not perfect circular form. Electron-phonon scattering at **K**/2<**q**<**K** is dominant because of large electron-phonon coupling (EPC) at this region. At **q**<**K**, although the strong EPC, the scattering effect is weak due to small portion. And at **q**~**K**, EPC is almost '0' [20].

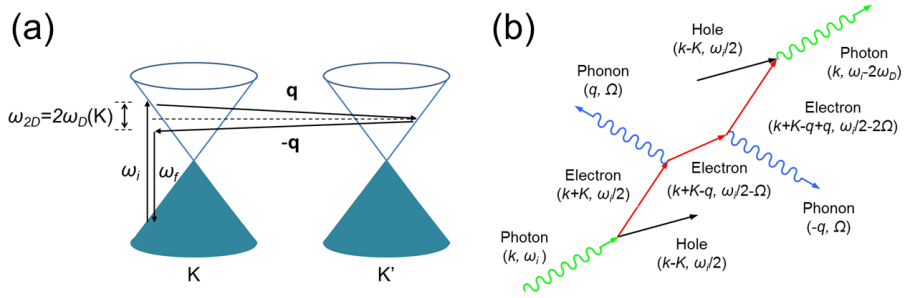

Figure 1.13. (a) A Schematic diagram of 2D-peak in Raman spectrum [20]. (b) Electron-hole pair creation and recombination in two phonon scattering.

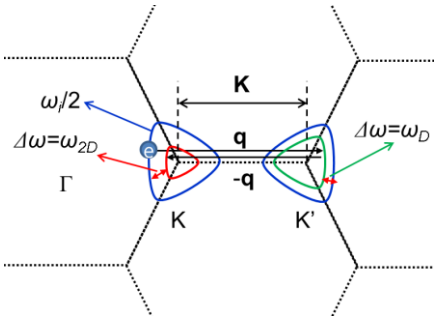

Figure 1.14. DR process and transition energy levels in trigonal warping system [20].

1.4.4 Phonon dispersion and Raman bands

The Raman shift values of graphene are concerned with phonon dispersion. This can be confirmed with matching of electron and phonon dispersion at the same wave vector (Fig. 1.15). Typical value of ω_G and ω_D of monolayer graphene are 1580 cm^{-1} and 1350 cm^{-1}. These are consistent with the large values in density of states of phonon. These can be different from other graphenes because of intrinsic doping.

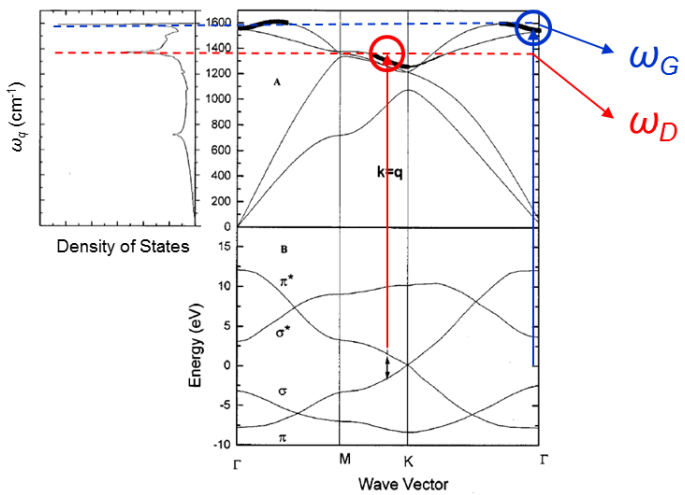

Figure 1.15. Electron energy band (below) and phonon dispersion (above) with phonon density of states of a monolayer graphene [21].

1.4.5 Raman spectrum of doped graphene

In doped graphene, there are three changes of Raman spectrum, G-peak shift, G-peak width decreasing and 2D-peak reduction.

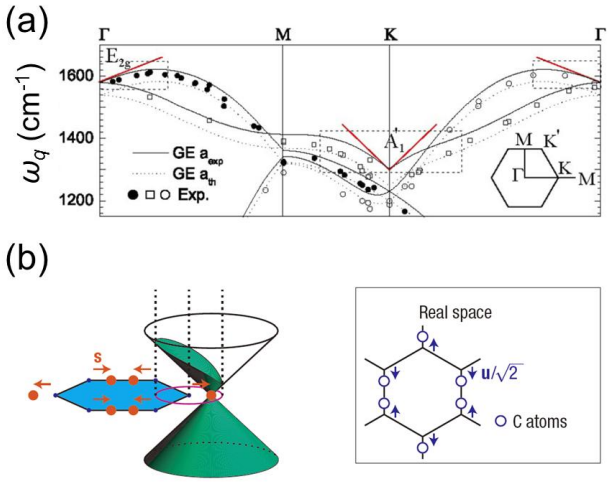

Figure 1.16. (a) Phonon dispersion of graphene. Kohn anomaly is indicated at K- and Γ-points [24]. (b) Electron band in the presence of lattice distortion which causes non -adiabatic deformation of electron system [23].

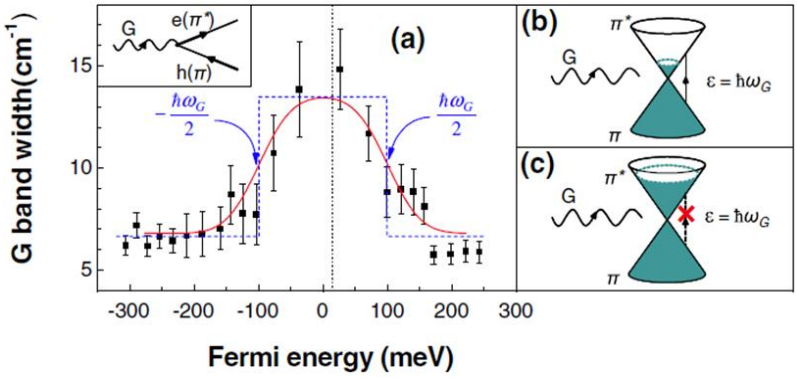

Figure 1.17. (a) G-band width variation with Fermi-level shift. (b) Allowed phonon decay into electron-hole pair. (c) Phonon decay into electron-hole pair is forbidden by Pauli exclusion principle [18].

First, it is known that G-peak shift is causes by removal of Kohn anomaly. Kohn anomaly is lattice vibration screening by the conduction electrons in metal [22]. This is occurred in graphene, graphite and metallic CNT as well as normal metal. As a result, the phonon frequency abruptly decreases at certain points. In graphene, Kohn anomaly is observed at K- and Γ-points which is shown in Fig. 1.16(a). If graphene is doped, electrons occupy the energy level and as doping increases, the Fermi-level (E_F) is elevated at the same time. Because of lattice vibration, Dirac point is deviated from atomic site and the electron distribution is distorted (Fig. 1.16(b)) which is increased as E_F elevation. If the electrons are in adiabatic condition, the electron distribution is rigid. However, in non-adiabatic case, electrons move with momentum relaxation time that is a reason of the distortion of electron distribution. Finally, E_F increasing with doping removes Kohn anomaly from K-point, and phonon frequency increases, which is related with the G-peak in Raman shift [23].

Second, G-peak sharpness is observed in doped graphene (Fig. 1.17(a)) [18]. The phonon with small wave vector ($\mathbf{q}\approx 0$) ,decayes into electron-phonon pair. However, the electron-hole pair creation is forbidden when $2E_F > E_{phonon}$ because of Pauli exclusion principle, As increasing E_F, the number of cases in phonon decay decreases. This causes the G-band width narrowing with doping (Fig. 1.17 (b), (c)).

Third, 2D-peak suppression is occurred with doping. The scattering between electron-phonon in DR process is reduced by electron-electron interaction. The scattering of photo-excited electron and hole with phonon is sensitive and this is related to intensity of 2D-peak [25].

1.5 Outline of Thesis

In this thesis, the transport properties of halogen-doped graphene were investigated with variation of halogen doping level. In particular, gate voltage-dependent resistance near Dirac point was studied in terms of the mobility, maximum resistance and the charge neutrality point shift. This thesis is organized as follows. The experimental method is described in Chapter 2.

Electrical properties of halogen-doped mono and multi-layer graphene are presented in Chapter 3. Here, the charge neutrality point shift, mobility change and maximum resistance variation are discussed. In Chapter 4, the doping effect is confirmed with Raman spectrum and AFM. Finally, in Chapter 5, we summarize our results and make conclusions.

Bibliography

[1] M. I. Katsnelson, *Materials today* **10**, 20 (2007)

[2] J. –H. Chen, C. Jang, S. Adam, M. S. Fuhrer, E. D. Williams, and M. Ishigami, *Nature Phys*. **4**, 377 (2008)

[3] F. Schedin, A. K. Geim, S. V. Morozov, E. W. Hill, P. Blake, M. I. Katsnelson, and K. S. Novoselov, *Nature Mater*. **6**, 652 (2007)

[4] C. Jang, S. Adam, J. –H. Chen, E. D. Williams, S. D. Sarma, and M. S. Fuhrer, *Phys. Rev. Lett*. **101**, 146805 (2008)

[5] J. –H. Chen, W. G. Cullen, C. Jang, M. S. Fuhrer, and E. D. Williams, Phys. Rev. Lett. **102**, 236805 (2009)

[6] F. Chen, J. Xia, D. K. Ferry, and N. Tao, *Nano Lett*. **9**, 2571 (2009)

[7] Y. Ohno, K. Maehashi, Y. Yamashiro, and K. Matsumoto, *Nano Lett*. **9**, 3318 (2009)

[8] K. Pi, K. M. McCreary, W. Bao, W. Han, Y. F. Chiang, Y. Li, S. –W. Tsai, C. N. Lau, and R. K. Kawakami, *Phys. Rev. B,* **80**, 075406 (2009)

[9] K. M. McCreary, K. Pi, A. G. Swartz, W. Han, W. Bao, C. N. Lau, F. Guinea, M. I. Katsnelson, and R. K. Kawakakmi, *Phys. Rev. B*, **81**, 115453 (2010)

[10] A. N. Rudenkoi, F. J. Keil, M. I. Katsnelson, and A. I. Lichtenstein, *Phys. Rev. B,* **82**, 035427 (2010)

[11] X. Fan, L. Liiu, J. –L. Kao, and Z. Shen, *J. Phys. Chem*. **114**, 14939 (2010)

[12] N. Y. Jung, N. D. Kim, S. Jockusch, N. J. Turro, P. Kim, and L. Brus, *Nano Lett*. **9**, 4133 (2009)

[13] G. Kalita, K. Wakita, M. Takahashi, and M. Umeno, *J. Mater. Chem*. **21**, 15209 (2011)

[14] S. Tongay, J. Hwang, D. B. Tanner, H. K. Pal, D. Maslov, and A. F. Hebard, *Phys. Rev. B*, **81**, 115428 (2010)

[15] S. Adam, E. H. Hwang, V. M. Galitski, and S. D. Sarma, *PNAS*, **104**, 18392 (2007)

[16] J. –H. Chen, C. Jang, S. Xiao, M. Ishigami, and M. S. Fuhrer, *Nature Nanotech*, **3**, 206 (2008)

[17] S. Y. Kim, J. H. Nah, I. S. Jo, D. Shahrjerdi, L. Colombo, Z. Yao, E. Tutuc, and S. K. Banerjee, *Appl. Phys. Lett*. **94**, 062107 (2009)

[18] J. Yan, Y. Zhang, P. Kim, and A. Pinczuk, *Phys. Rev. Lett*, **98**, 166802 (2007)

[19] A. C. Ferrari, *Solid State Comm*. **143**, 47 (2007)

[20] A. C. Ferrari, J. C. Meyer, V. Scardaci, C. Casiraghi, M. Lazzeri, F. Mauri, S. Piscanec, D. Jiang, K. S. Novoselov, S. Roth, and A. K. Geim, *Phys. Rev. Lett*. **97**, 187401 (2006)

[21] A. C. Ferrari, and J. Robertson, *Phys. Rev. B*, **61**, 14095 (2000)

[22] W. Kohn, *Phys. Rev. Lett*. **2**, 393 (1959)

[23] S. Pisana, M. Lazzeri, c. Casiraghi, K. S. Novoselov, A. K. Geim, A. C. Ferrari, and F. Mauri, *Nature Mater*. **6**, 198 (2007)

[24] S. Piscanec. M. Lazzeri, F. Mauri, A. C. Ferrari, and J. Robertson, *Phys.*

Rev. Lett. **93**, 185503 (2004)

[25] D. M. Basko, S. Piscanec, and A. C. Ferrari, *Phys. Rev. B*, **80**, 165413 (2009)

Chapter 2

Experimental

Graphene layers length of few micrometers were extracted by mechanical exfoliation with 3M tape. The number of graphene layers was characterized with Raman spectrum as the ratio of 2D- and G-peak intensity. For electrical measurement, graphene field effect transistors were fabricated by standard e-beam lithography process. Halogen doping was performed in a glass doping tube. In order to measure the gate-dependent resistance of graphene, the 4-probe and 2-probe methods were used. Doping and electrical measurement were performed in a high vacuum (~10^{-5} Torr) at room temperature.

2.1 Grahene extraction and device fabrication

Graphene layers were obtained by mechanical exfoliation method from Natural Graphite (Madagascar flakes from NGS) or HOPG. It was deposited on highly *p*-doped silicon substrate (100) (ρ<0.005Ω cm which is covered with thermally grown SiO_2 thickness of 300 nm) (Fig. 2.1(b)). The Si/SiO_2 substrate is pre-patterned by photolithography so as to make coordinates for finding location of exfoliated graphene (Fig. 2.1(a)). The distances between the coordinates are 100μm, which are useful as align marks in e-beam lithography. Graphene was characterized with optical microscope and Raman spectroscopy as the ratio of the G- (doubly degenerated E_{2g} mode) to 2D-peak (double resonant electron-phonon scattering) intensity [1]. The full width half

maximum (FWHM) of 2D-peak also gives the information for number of layers of graphene. For monolayer graphene in Fig. 2.2, FWHMs are about 26 cm^{-1} .

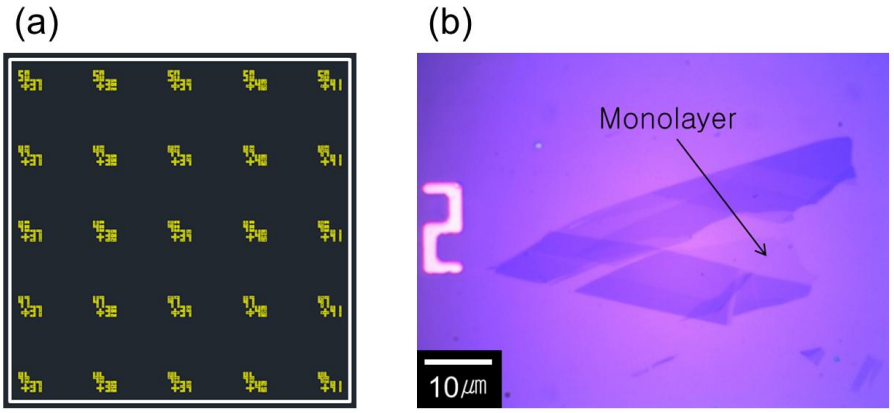

Figure 2.1. (a) A part of mask pattern in pre-patterned Si/SiO_2 substrate. The distances between the coordinates are 100μm. The positions of graphene are found by using XY coordinates on the substrate. (b) The exfoliated graphene layers are on the Si/SiO_2 substrate.

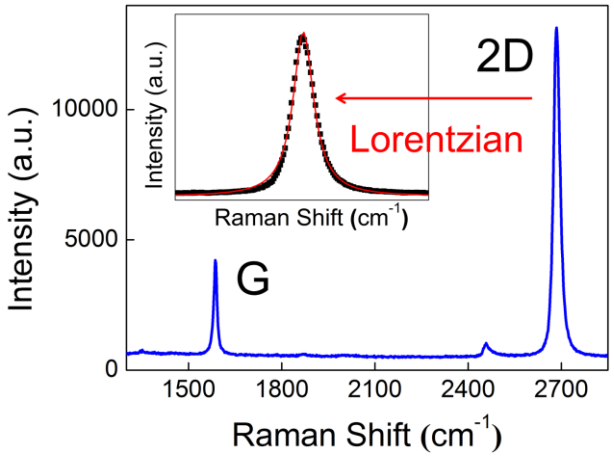

Figure 2.2. Raman spectrum of pristine monolayer graphene. Inset shows a single peak fitting with Lorentzian of 2D-peak.

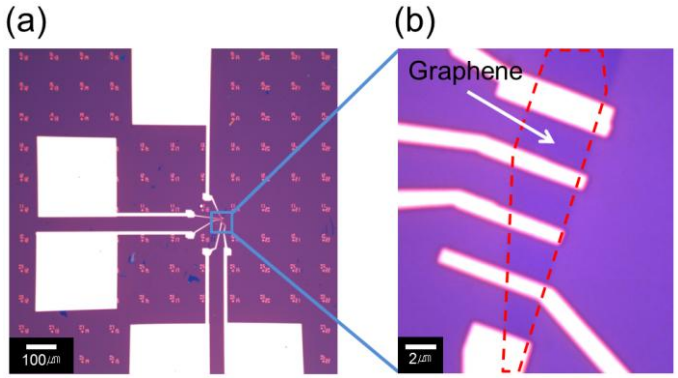

Figure 2.3. (a) A graphene device fabricated by standard e-beam lithography on Si/SiO_2 substrate. (b) A magnification of a fabricated device in figure (a).

For device fabrication, a series of electrodes was patterned by standard e-beam lithography process. Cr/Au (3/30nm) or Ti/Au (5/50nm) was deposited by thermal evaporation or e-beam evaporation for electrical contact.

2.2 Halogen Doping

In order to measure the doping effect, first, the devices were annealed in a high vacuum (~10^{-5} Torr) at T~145 ℃ in a glass tube by halogen lamp radiation heating. Second, graphene was doped with I_2 and Br_2 vapor in a glass doping tube. Before doping, I_2 (Siegmar Aldrich, purity of 99.999%, Anhydrous) and Br_2 (Siegmar Aldrich, purity of 99.5+%, A.C.S. regent) were purified with evacuation which is a repetitive sequence (5 times) of freezing and thawing (Fig. 2.4). If the vapor is frozen, there is no gas and liquid in a source tube. As temperature increasing, the dissolved contaminants diffuse into the tube, and the molecules can be removed by evacuation.

Figure 2.5 (a) shows a picture of doping setup. Halogen doping is confirmed in glass doping tube. The sample is mounted under the chip connector (Fig. 2.5 (b)). Sample mounting location is important because the halogen vapor goes from source tube (right side of the picture) to low pressure part (left side of the picture) by evacuation. As the vapor passed doping line,

the molecules are adsorbed on graphene. However, if the sample is located under the horizontal line that is source input line, the molecules will not be reached the sample. The sample mounting part is displayed in Fig. 2.5(b). Schematic diagram of halogen doping setup is represented in Fig. 2.6. Since the halogen molecules have high vapor pressure (I_2 : 0.231 mmHg at 25 ℃, Br_2 : 175 mmHg at 20 ℃), the temperature of source tube was reduced by cooling with dry ice and ethyl alcohol mixed liquid (T~-77 ℃). Finally, the back gate-dependent resistance was measured at room temperature (T=22 ℃).

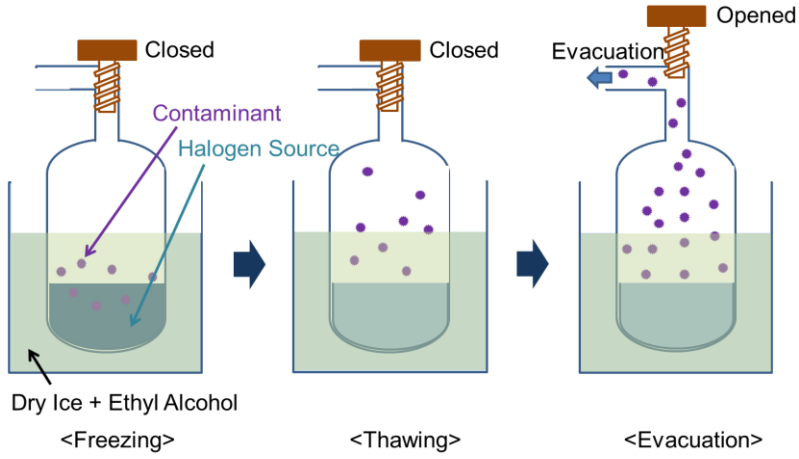

Figure 2.4. Purification of halogen molecules before doping by evacuation with a sequence of freezing and thawing.

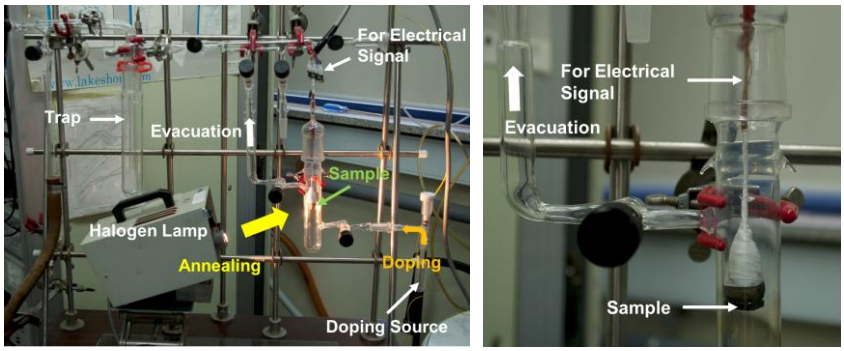

Figure 2.5. (a) A picture of doping setup. Halogen doping is confirmed with glass doping line. (b) The samples are mounted under the chip connector.

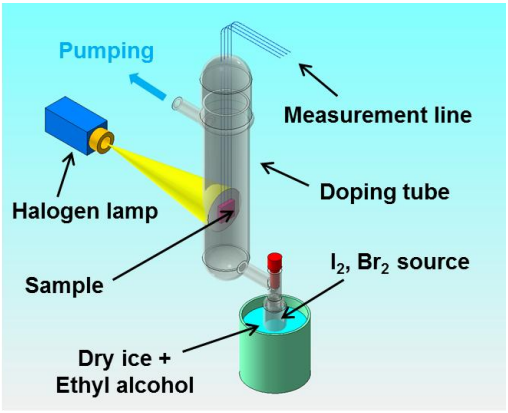

Figure 2.6. A schematic diagram of halogen doping setup. Graphene is annealed with heating by a halogen lamp. In order to control vapor pressure of the molecules, the source tube is cooled by dry ice and ethyl alcohol mixture.

2.3 Electrical Measurement

For 4-probe resistance measurement, the constant excitation current was flown (10~100 nA) in graphene channel with external resistance of 10MΩ. The potential drop between voltage probe was measured with lock-in amplifier (EG&G 5210). The 2-probe resistances were obtained from the relation with the inverse of channel current measured by Semiconductor characterization system (SCS-4200, Keithley Instrument, Cleaveland, OH, USA). The back gate voltage was applied with a model 6517A1 electrometer (Keithley Instrument, Cleaveland, OH, USA). Gate voltage-dependent resistances were measured in a glass doping tube at same condition with halogen doping.

2.4 Raman spectroscopy

Raman spectrum of mono and multi-layer graphene is obtained by using micro-Raman system with Ar-ion laser of 514 nm (LabRaman HR, Horiba Jobin-Yvon, France). The exposure power is 0.5mW and the exposure time is 60s. The Raman measurement was performed at room temperature in air.

Bibliography

[1] A. C. Ferrari, J. C. Meyer, V. Scardaci, C. Casiraghi, M. Lazzeri, F. Mauri, S. Piscanec, D. Jiang, K. S. Novoselov, S. Roth, and A. K. Geim, *Phys. Rev. Lett*. **97**, 187401 (2006)

Chapter 3

Electrical Properties of Halogen-doped Mono and Multi-layer Graphene

3.1 Results and Discussion

Here we studied the back gate voltage (V_g)-dependent resistance of graphene layer upon exposure of halogen molecules (I_2 and Br_2). Several distinct effects of halogen doping in mono and multi-layer graphene are observed as compared to those of other dopants in previous studies.

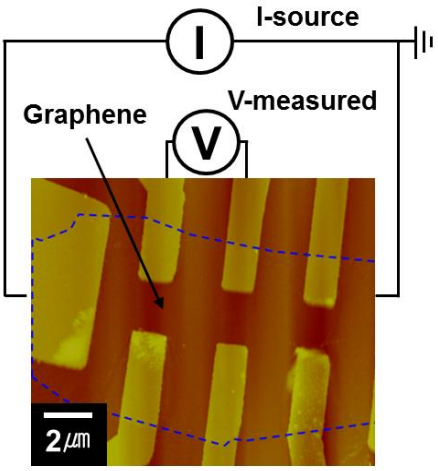

Figure 3.1. An AFM image of a graphene device and a measurement scheme. The dashed line indicates the edge of graphene.

An AFM image and a 4-probe measurement scheme are displayed in Fig. 3.1. Figure 3.2 shows the Dirac voltage (V_D) shift as a function of time after I_2-doping at each degree of doping. V_D is a gate voltage if the Fermi-level is positioned at charge neutrality point (CNP) and V_0 is a Dirac voltage of annealed graphene. For each degree of doping, we kept the exposure time of I_2 vapor less than 1 second in order to avoid over-doping. As I_2 doping, the doping chamber is evacuated while monitoring the gate-dependent resistances. In case of lightly doping, since I_2 is adsorbed more as time passed, the V_D increases until 10 minutes after valve opening until it is saturated. On the contrary, the V_D initially decreased as time passed at highly doped condition until 30 minutes. Because I_2 doping is physisorption, the molecules adsorbed weakly (Van der Waals interaction) [1] and unstable molecules are desorbed with evacuation.

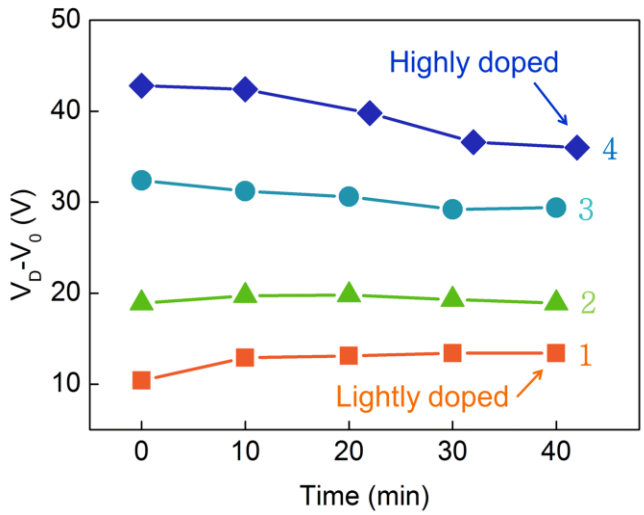

Figure 3.2. Dirac voltage (V_D) shifts with respect to evacuation time after I_2 doping at each doping level. V_D is a gate voltage if the Fermi-level is positioned at charge neutrality point (CNP). V_0 is V_D of undoped graphene.

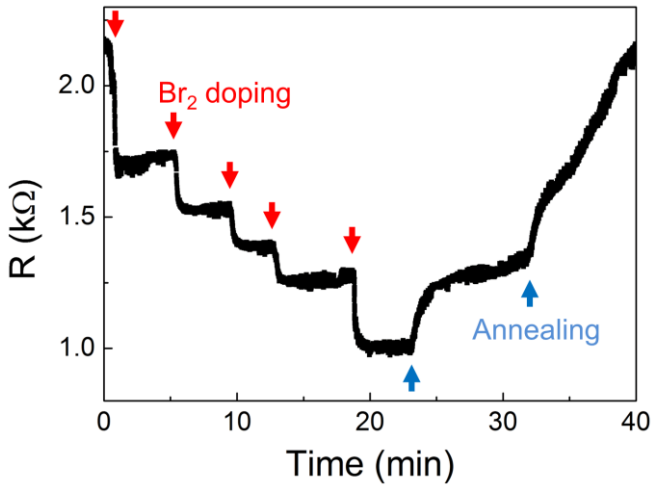

Figure 3.3. In-situ resistance of Br_2-doped monolayer graphene at *Vg*=0 V. The red and blue arrows indicate the Br_2-doping and annealing points, respectively.

We present the in-situ resistance of Br_2-doped monolayer graphene at V_g=0 V (Fig. 3.3). The red and blue arrows indicate the Br_2 doping and annealing points. If we dope the graphene, the resistance decreases step by step. At each step, the resistance increases slightly as time passed due to evacuation. When the device is started to be annealed (first annealing point), the resistance increases due to dedoping. At higher temperature (second annealing point), the resistance increases until it reach initial value. From this, the possibility of device recovery is observed by annealing. It was shown in I_2-doped graphene, too.

Figure 3.4 shows the gate-dependent resistances measured at room temperature in a high vacuum (~10^{-5} Torr). The measurement was carried out after Dirac voltage (V_D) saturation in Fig. 3.4. Prior to chemical doping, V_0 is 4.6V. It is affected by remained *p*-type dopants such as water, oxygen and residue of lithography process. There are three main halogen doping effects. First, the V_D shifts to more positive gate voltage. It means that, as doping, the electrons transfer from graphene to I_2 because of larger electronegativity of I_2 than that of graphene [2-4]. It is well known that the hole doping is caused by the higher electronegativity of I_2 than that of carbon materials such as carbon

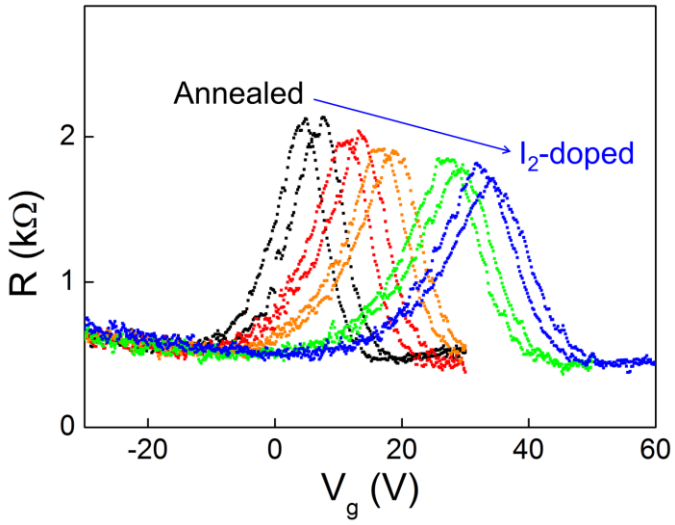

Figure 3.4. The gate-dependent resistances of I_2-doped monolayer graphene at room temperature in a high vacuum (~10^{-5} Torr). As the graphene is doped subsequently, the maximum resistance (R_{max}) is shifted to positive voltage.

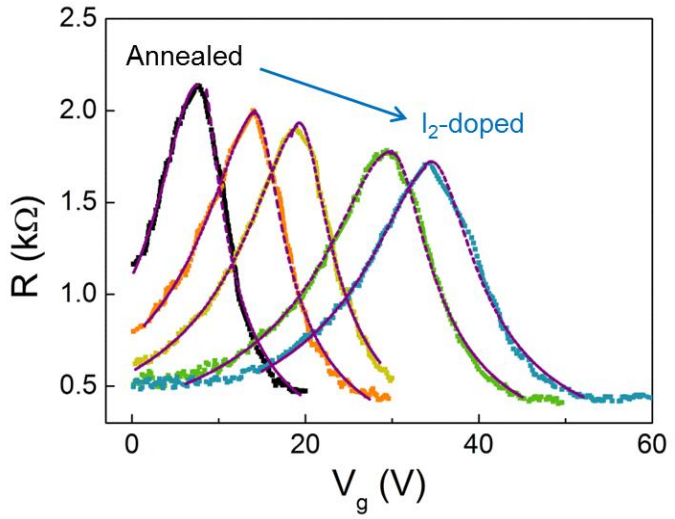

Figure 3.5. The data of forward sweep direction in Fig. 3.4. The dashed lines are fitting curves calculated by $R=(L/W)/e\mu(n_g^2+n_0^2)^{1/2}=(L/W)/e\mu(\alpha^2(V_g^2-V_0^2)+n_0^2)^{1/2}$, where L, W, μ, n_g, n_0 and V_0 are channel length, channel width, carrier mobility, gate induced carrier density, residual carrier density and the gate voltage of R_{max}, respectively.

nanotube, fullerene, graphite, polyacetylene and pentacene. Secondly, the graphene mobility decreases as increasing doping level. It is a typical result of doped graphene. Lastly, the hysteresis is observed, a result of charging effect by charge trap or capacitive charging [5, 6].

Figure 3.5 is the forward gate sweep data is chosen from Fig. 3.5 because the gate-dependent resistance shows anisotropy in the electron- and hole-doped regions. The asymmetry resistance is fitted by the equation of

$$R = \frac{L/W}{e\mu\sqrt{n_g{}^2 + n_0{}^2}} = \frac{L/W}{e\mu\sqrt{\alpha^2(V_g - V_D)^2 + n_0{}^2}} \tag{3.1}$$

at each carrier regime with mobilities, μ_e and μ_h, which are represented by dashed lines (Fig. 3.5). Where, L, W, μ, n_g and n_0 are channel length, channel width, carrier mobility, gate-induced carrier density and residual carrier density. μ_e and μ_h of undoped graphene are 7830 and 4470 $cm^2V^{-1}s^{-1}$. The gate-induced carrier density is

$$n_g = \frac{c_g(V_g - V_D)}{e} = \alpha(V_g - V_D)\,,$$

where c_g (1.15×10^{-4} F/m^2) is capacitance per unit are of 300 nm SiO_2 and $\alpha = 7.2 \times 10^{10}$ $V^{-1}cm^{-2}$. The n_0 related with R_{max} is caused by electron-hole puddle induced by the impurities [7]. The observed resistance is an inverse form of linear conductivity due to charged impurity scattering. As graphene is doped, the mobility is reduced by scattering with the impurities, the charged impurities and halogen-induced impurities. Interestingly, the R_{max} is found to be reduced with doping, which is opposite to what found in the previous studies with other types of dopants [8-11].

The graphene device with I_2 doping is illustrated schematically in Fig. 3.6. The adsorbed I_2 molecules are in the form of I_3^- or I_5^- (Fig. 3.6), which is already well known from the Raman studies [2-4]. This is also observed in the case of CNT, fullerene, graphite, polyacetylene and pentacene. The I_2 molecules give holes to carbon atoms. Fermi-level is shifted to the hole carrier

regime if the graphene is doped with halogen molecules. Figure 3.7 shows the Fermi-level modulation by doping. The π- and π^*-band play a role of valence and conduction band in graphene, respectively. If the graphene is hole doped, Fermi-level is shifted to hole carrier regime and the density of states at Fermi-level increases. This is the reason of conductivity increasing.

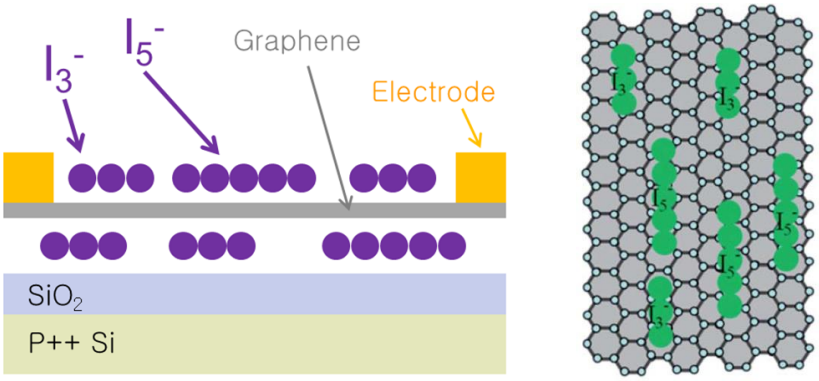

Figure 3.6. (a) A Schematic diagram of I_2-doped graphene device (left). I_2 adsorbed on graphene is formed the iodine anion, I_3^- and I_5^-, which gives holes to carbon atoms (right) [3].

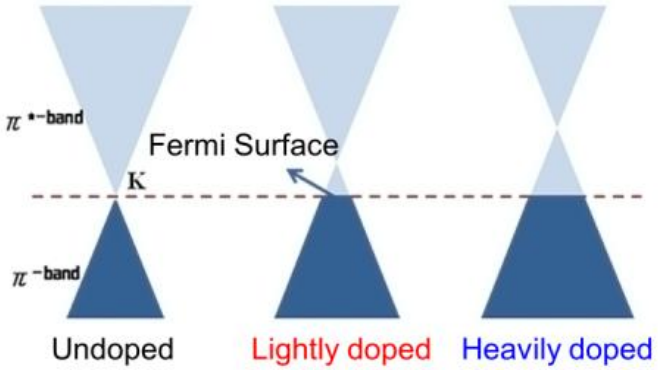

Figure 3.7. The Fermi-level modulation by doping. As doping level increases, the Fermi-level is shifted to π-band.

As shown in energy band diagram in Fig 3.7, conduction band and valence band is connected at just one point, Dirac point, which is zero density of states. In fact, however, the measured conductivity is not zero. This indicates the existence of charge carriers which contribute the current flow. The non-zero conductivity is due to spatially multiform charge distribution, electron-hole puddle, which is caused by inhomogeneous potential fluctuation induced by the charged impurities embedded on substrate [7, 12]. Thus, this point is called charge neutrality point (CNP) rather than Dirac point. In monolayer graphene, non-zero conductivity is predicted theoretically as $4e^2/\pi h$. However, it depends on the quality of measured samples from $2\sim10e^2/h$ on SiO_2 [12]. In pristine monolayer graphene, before I_2 doping, the minimum conductivity (σ_{min}) is $6e^2/h$.

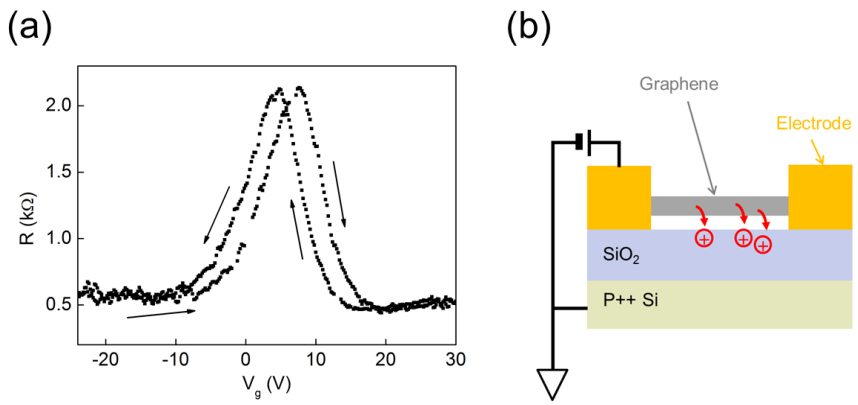

Figure 3.8. (a) Hysteresis of gate-dependent resistance of monolayer graphene. (b) It is caused by capacitive charging effect such as avalanche injection from graphene to SiO_2 dielectric layer by applied gate voltage.

The graphene is sensitive to external contamination and there are charge traps and defects. These are causes of hysteresis in gate-dependent resistance. When we measure the gate-dependent resistance in graphene, the hysteresis is observed (Fig. 3.8 (a)). The gate voltage is swept in the direction of 0 V → 30V → 0 V → –30 V → 0 V. When the sweep is returned at 30V, the resistance is decreased (negative hysteresis). This is explained with capacitive charging or transient charging effect such as avalanche injection (Fig. 3.8(b))

[5, 6]. If the hysteresis is positive, it is described with dipole interaction by water or oxygen molecules [5].

Figure 3.9 displays the gate-dependent resistance of Br_2-doped monolayer graphene. As the Br_2 is adsorbed on graphene surface, the V_D shifts to the hole carrier regime due to electronegativity of Br_2 as found in the case of I_2 doping. The mobility reduction and R_{max} decreasing are also observed, which are consistent with what found in the I_2-doped graphene. Therefore, it is expected that the scattering mechanism of Br_2-doped graphene is similar with that of I_2-doped one.

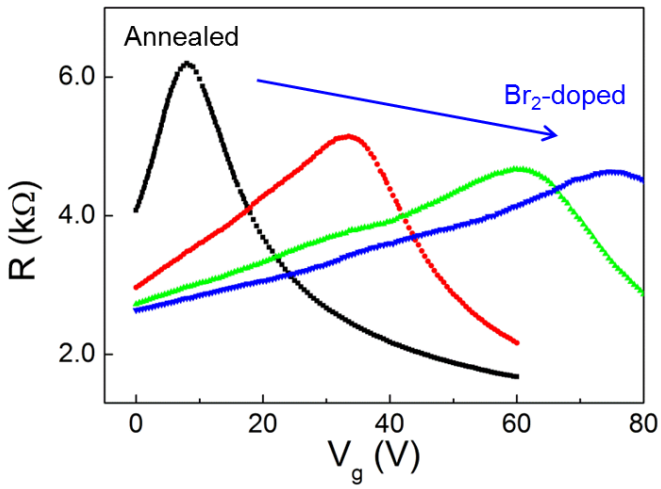

Figure 3.9. The gate-dependent resistance of Br_2-doped monolayer graphene at room temperature.

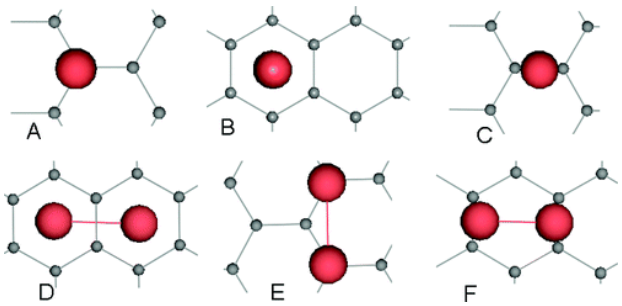

Figure 3.10. High symmetry adsorption for Br_2 molecules on graphene. (a)~(c) are perpendicular and (d)~(f) are parallel adsorption to graphene sheet [13].

	Perpendicular-to-graphene			Parallel-to-graphene		
	A	B	C	D	E	F
Binding energy (meV)	460	210	311	213	183	177
Bond length (Å)	2.309	2.281	2.305	2.268	2.270	2.270
Distance from graphene (Å)	2.80	3.011	2.809	3.325	3.416	3.416

Table 3.1. Binding energy, bond length (Br-Br) and the distance between Br_2 and graphene [13]

It is expected that Br_2 is adsorbed in the form of not Br anions but Br_2 molecules, homo-polar molecule. Figure 3.10 shows the 6 high symmetry adsorption sites calculated by DFT for Br_2 molecules on graphene [13]. (a)~(c) are perpendicular adsorptions and (d)~(f) are parallel adsorptions. The binding energy, bond length of Br_2 and the distance between Br_2 and graphene are calculated by DFT (Table 3.1) [13]. The binding energy of 'A' adsorption site is largest. In fact, the Br_2 molecules can be adsorbed in various forms not only the six high symmetries but also other forms. From this theoretical prediction, we expect the order of adsorption constants quantitatively.

If we compare the mobility of halogen-doped graphene with the result of another doping, it is more helpful to explore the scattering mechanism (Fig. 3.11). The electron and hole mobility of I_2-doped graphene are decreased by doping. The mobility reduction of I_2-doped graphene is smaller than that of K and Au doping. This is due to a screening effect of charged impurity scattering by halogen molecules intercalated between graphene and SiO_2. The intercalated I_2 molecules underlying graphene screen the impurity potential, thus the carrier scattering by the charged impurities are reduced. As a result, the mobility reduction becomes smaller than other types of doping. In the same way, in Br_2 doping, the small decreasing of mobiltiy is observed too. In case of graphene with low quality, the mobility change with doping is not significant. Because of initially generated impurities, the additional scattering effect is not large [8]. In case of Ti, Pt and Fe doping, the mobility reduction is negligible compared to another doping because of their small mobility.

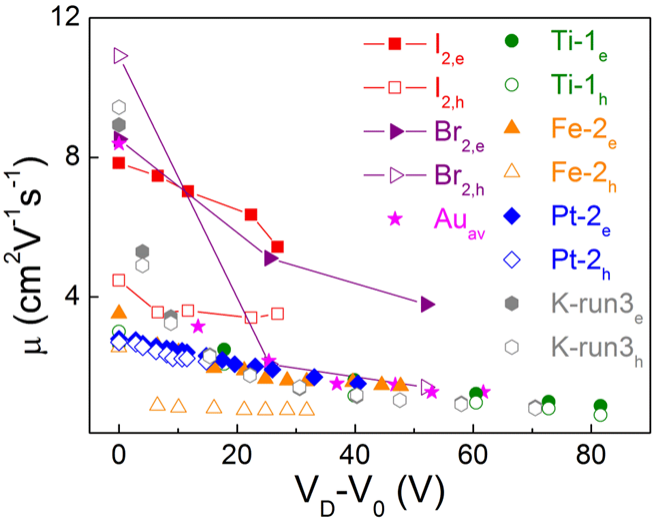

Figure 3.11. Electron and hole mobility values of doping by various dopants with respect to Dirac voltage shift (V_D-V_0). Mobility changes of I_2 and Br_2-doped graphene are represented by line and symbol. The data points of Au, Ti, Pt, Fe and K are obtained from the result of other reports [8-10].

The normalized mobility (μ/μ_0) (Fig. 3.12) and the normalized average mobility ($<\mu>/<\mu_0>$) (Fig. 3.13) of doping by various dopants with respect to Dirac voltage shift (V_D-V_0) are represented, where $<\mu>=(\mu_e+\mu_h)/2$. Potassium exhibits the strongest dependence with doping and halogen molecules show the weakest scattering behavior.

The relationship of scattering and various dopants is investigated in Fig. 3.14. Dirac voltage shift (V_D-V_0) vs. $1/\mu$-$1/\mu_0$ for doping with I_2 and Br_2 together with results for other dopants is displayed. The scattering effect is analyzed through power law relation of V_D-V_0~$(1/\mu$-$1/\mu_0)^b$~$(\Gamma)^b$, where Γ is total scattering rate. For point-like charged impurities with $1/r$ Coulomb interaction, the exponent b is expected to be b=1.2~1.3 as indicated by grey. For various dopants such as K and Au, b=1.3 was experimentally confirmed, while b<1.0 was observed for doping with Ti, Pt and Fe due to clustering of dopants.

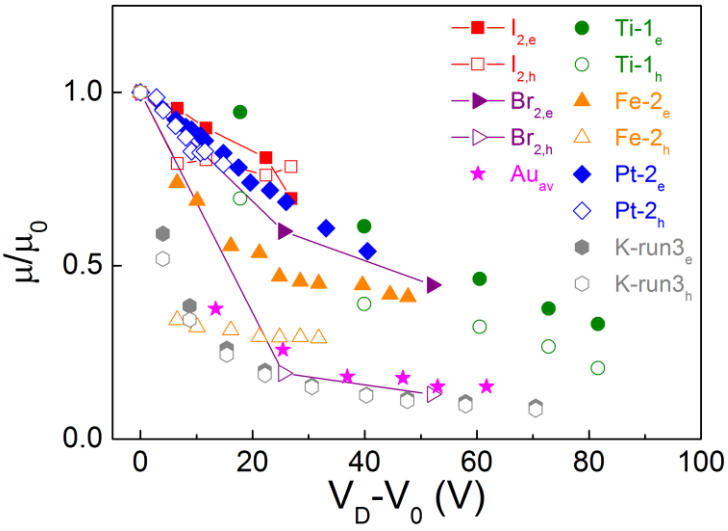

Figure 3.12. The normalized mobility (μ/μ_0) of doping by various dopants with respect to Dirac voltage shift (V_D-V_0). The data points of Au, Ti, Pt, Fe and K are obtained from the result of other reports [8-10].

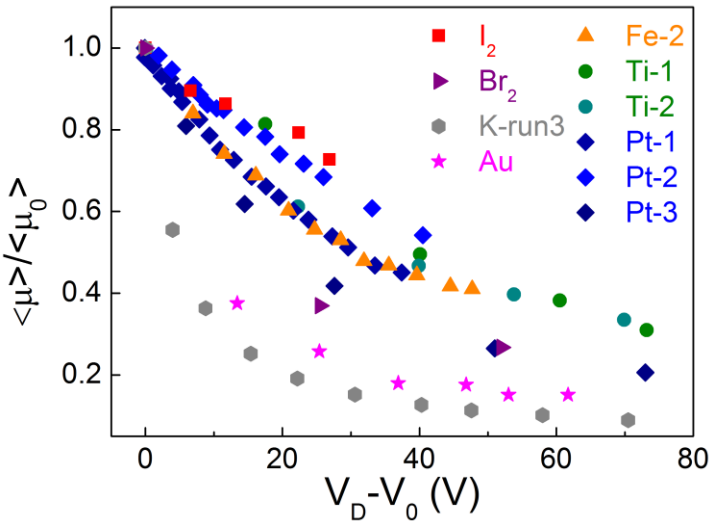

Figure 3.13. The normalized average mobility ($<\mu>/<\mu_{0>}$) of doping by various dopants with respect to Dirac voltage shift (V_D-V_0). The data points of Au, Ti, Pt, Fe and K are obtained from the result of other reports [8-10].

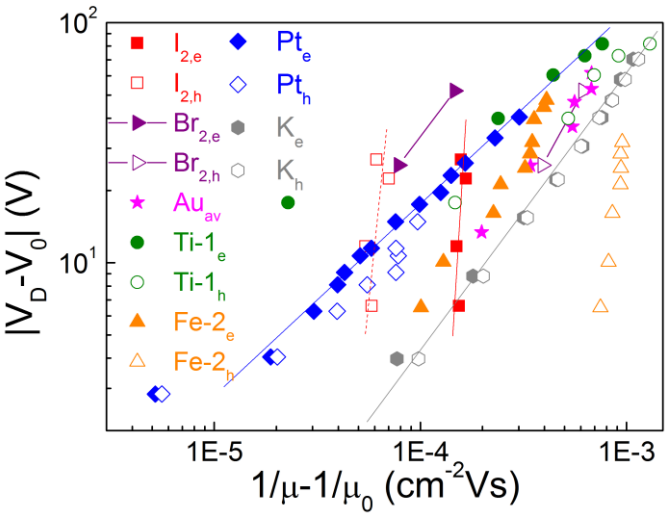

Figure 3.14. Dirac voltage shift (V_D-V_0) vs. $1/\mu$-$1/\mu_0$ of halogen doping with the data from doping with various dopants [8-10]. The guide lines show power law relation, V_D-V_0~$(1/\mu$-$1/\mu_0)^b$, associated with scattering rate induced by the impurities. μ_e and μ_h of I_2-doped graphene are represented by red squares (b=17.8) and empty squares (b=11.8). The blue dashed lines show the result of Pt doping (b=0.83~0.85). The grey line is power law fitting due to the scattering with point-like charged impurities (b=1.3).

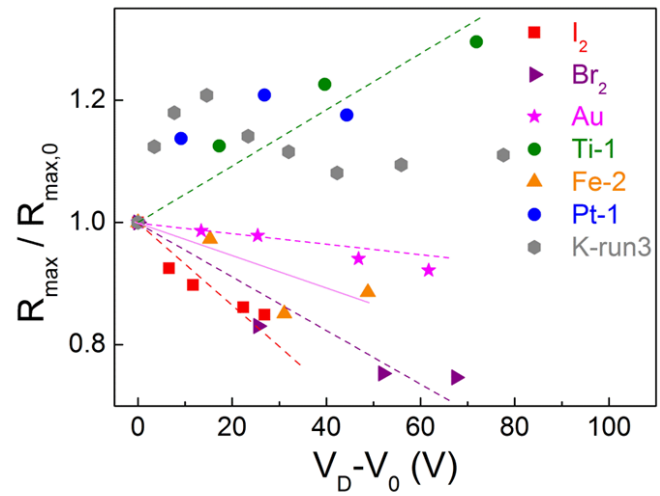

Figure 3.15. The normalized maximum resistance ($R_{max}/R_{max,0}$) of monolayer graphene doped with various dopants, where $R_{max,0}$ is R_{max} of undoped graphene. The dashed guide lines correspond to I_2 (red), Br_2 (purple), Au (magenta) and Ti doping (green), respectively [8-10].

In I_2 doping, however, larger values of exponent (b=17.8) is found weaker reduction of mobility by I_2 doping (Fig. 3.14). In Br_2-doped graphene, the relation between V_D-V_0 and $1/\mu$-$1/\mu_0$ is also different from doping with other materials. Recent investigation in I_2-doped graphene in fact revealed that when I_2 molecules were exposed to graphene on SiO_2 layer, they tend to be intercalated under the graphene layer. As I_2 molecules are intercalated, the Coulomb interaction is screened, a cause of reduced scattering with the charged impurities residing in the SiO_2 dielectric layer. Thus the mobility reduction becomes small. This effect is analogous to long range interaction of potential screening in dielectric medium in Fig. 1.6 [14].

Other anomalous effects of halogen doping can be found in the doping dependence of the R_{max} at the CNP. Figure 3.15 shows normalized R_{max} ($R_{max}/R_{max,0}$) as a function of V_D-V_0 for various dopants, where $R_{max,0}$ is R_{max} of undoped (annealed or pristine) graphene. For Ti and Pt doping, the $R_{max}/R_{max,0}$ increased with doping while for Au- and Fe-doped graphene, the $R_{max}/R_{max,0}$ remains almost constant.

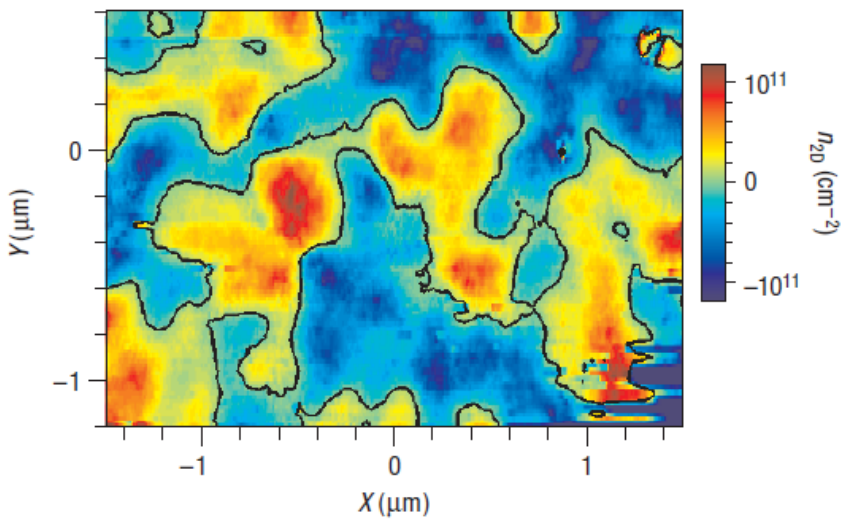

Figure 3.16. Charge distribution on graphene by inhomogeneous potential fluctuation due to the charged impurities embedded on SiO_2 [7].

In strong contrast, for halogen doping, R_{max} decreasing are shown. It can be understood as an effect of n_0 increasing in halogen doping. The resistance at CNP, R_{CNP}, is represented as

$$R_{CNP} = \frac{1}{\mu n_0 e}. \tag{3.2}$$

Even though mobility is reduced, n_0 increases with halogen doping. This is opposite to dielectric screening. Electrons of graphene in dielectric medium have higher mobility and small n_0 compared with n_0 in dielectric medium. Therefore, we can find out the difference of halogen doping compared with other doping. Halogen doping is not dielectric screening effect, is not purely charged impurity scattering effect and is not defect scattering effect which is introduced in chapter 1.2. From the result of mobility, R_{max} change and CNP shift, we can interpreted halogen doping as the charged impurity scattering which gives the more electron-hole puddle density. The impurities can be on both of graphene and SiO_2. This is very distinctive behavior that is difficult to separate to individual effect. The residual carrier density was measured by J. Martin et al. [7] (Fig. 3.16).

These results clearly demonstrate that halogen doping is distinct from doping with other dopants in many respects, not only the type of the induced carriers but also the detailed effects on the transport properties, which is related to the unique characters of halogen doping.

In order to confirm the aforementioned explanation, we performed the I_2 doping experiments on the monolayer graphene with its edge covered with a polymer layer that prevents I_2 molecules from being intercalated below the graphene layer. As shown in the inset of Fig. 3.17, the graphene device is covered by PMMA with a window-opened for the central region of the graphene layer for selective doping. In this figure, the gate-dependent resistance of I_2-doped monolayer graphene that is PMMA window-patterned is shown. From this, it is expected to reduce the scattering by the charged impurities embedded on SiO_2. As a result, R_{max} increasing is observed with I_2 doping. However, the V_D shift was not observed in PMMA-covered region.

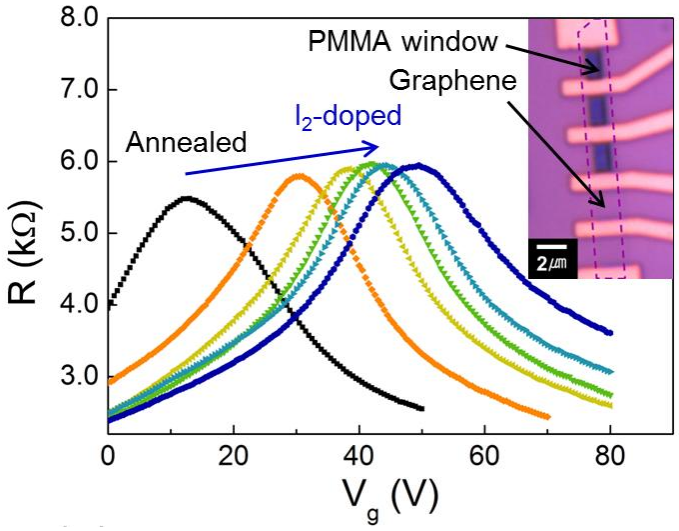

Figure 3.17. The gate-dependent resistance of I_2-doped monolayer graphene with its edge covered by PMMA. The central region of the PMMA-covered graphene is opened (dark colored region in device) for selective doping. Inset shows an optical microscope image of a PMMA window-opened graphene device. The dashed line indicates the graphene edge. The I_2 molecules are prohibited to intercalate between graphene layer and SiO_2.

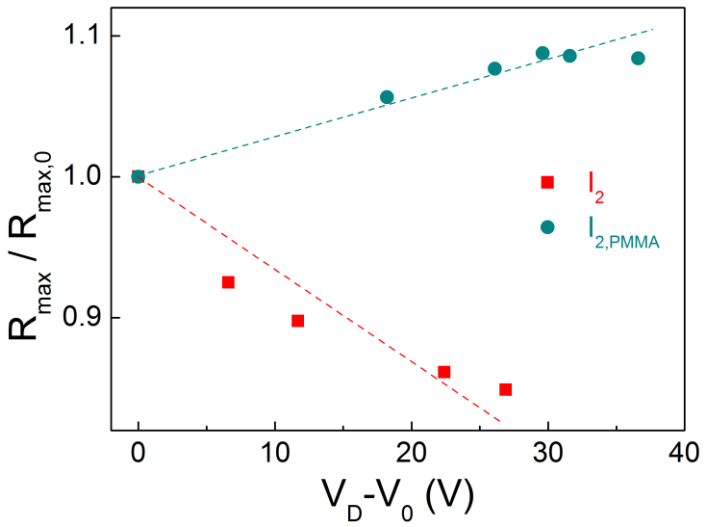

Figure 3.18. The normalized resistance ($R_{max}/R_{max,0}$) of I_2-doped monolayer graphene. The R_{max} of PMMA window-opened graphene increases, which is a different behavior from the result of graphene with no PMMA layer.

Since the I_2 molecules are prevented to be intercalated into under the graphene, the carrier transport is affected by the charged impurities on graphene. As a result, R_{max} increases with doping. This is shown in Fig. 3.18, a comparison between I_2-doped graphene with PMMA window and no window.

Temperature-dependent resistivity of I_2-doped monolayer graphene is measured in the region of $V_g \neq V_{CNP}$. When gate voltage increases to electron and hole regime, the resistivity changes are observed, respectively. This is consistent with the *p*-doping result. However, as temperature increases, resistivity decreases. It is opposite behavior to the result of undoped graphene on SiO_2 [15], which shows a scattering effect with optical phonon on SiO_2. Thus, we consider the resistance decreasing with temperature as an effect of halogen doping. Although the resistance change is not drastic, it has an analogy with insulating behavior. However, because grapene is a metal at $V_g \neq V_{CNP}$, it is difficult to interpret as a metal-insulator transition.

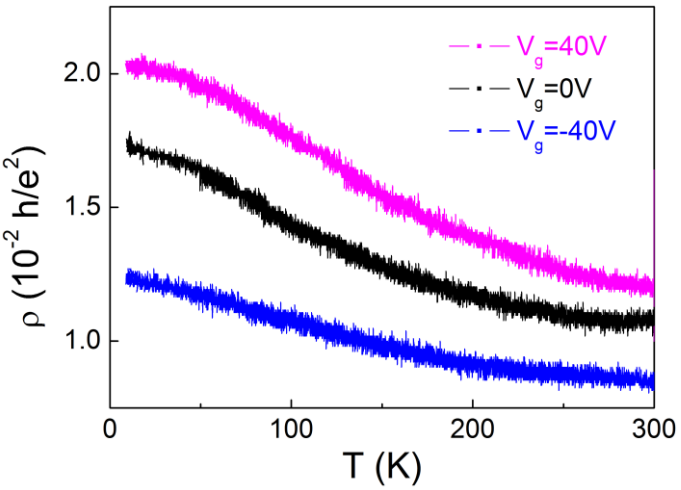

Figure 3.19. Temperature-dependent 4-probe resistivity of I_2-doped monolayer graphene. The resistivity decreasing is understood as a halogen doping effect.

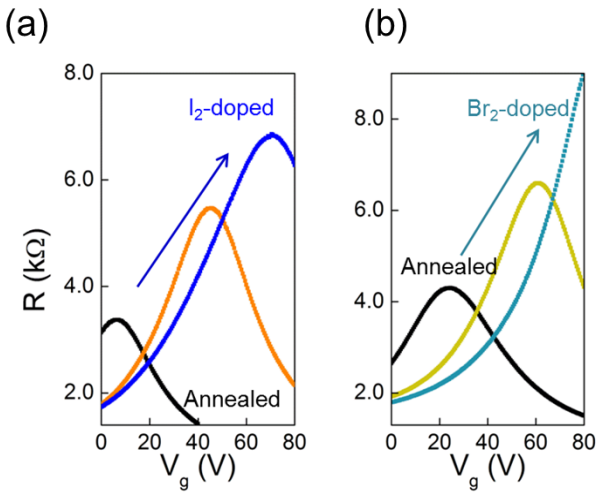

Figure 3.20. The gate-dependent resistances of halogen-doped multi-layer graphene. In contrast to monolayer, R_{max} increases with doping.

On the contrary, the R_{max} enhancement is observed in I_2- and Br_2-doped multi-layer graphene, which is opposite to what found in monolayer graphene (Fig. 3.20). In multi-layer graphene, the molecules can be intercalated into graphene layers or adsorbed on the edge of graphene layers as well as can be adsorbed on the surface. Thus we expect that screening effect is weaker than the result of doping on monolayers. However, it is not clear interpretation of doped multi-layer graphene. In order to explain the halogen doping on multi-layer graphene, we need further experimental and theoretical studies.

Figure 3.21 shows the gate-dependent resistance of Br_2-doped multi-layer graphene with its edge covered by PMMA. The dark region indicates the window-opened region for selective doping. When we dope multi-layer graphene, CNP was shifted to hole carrier regime also. Owing to mobility reduction near charge neutrality point, R_{max} increases. Because the Br_2 molecules are prevented to be intercalated into graphene layers and underlying graphene, there is weak scattering effect by the charged impurities embedded on SiO_2.

Dedoping with evacuation time of I_2-doped bi-layer graphene is measured (Fig. 3.22). Current decreasing is observed as expected. In contrast to

monolayer, current saturation time is more than 100 min. This is interpreted that intercalation is a stronger binding than surface adsorption.

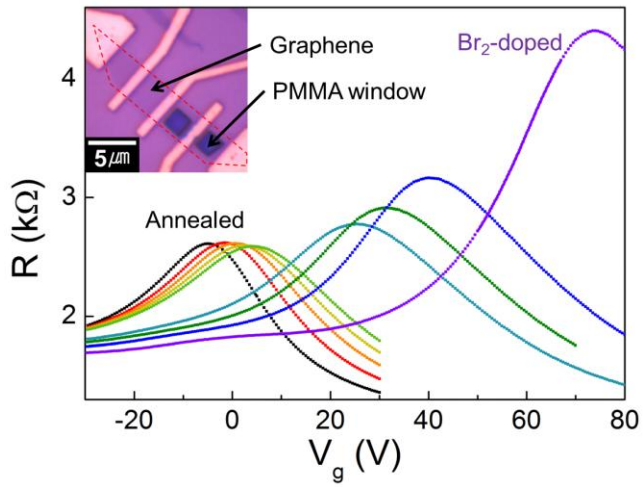

Figure 3.21. Gate-dependent resistance of Br_2-doped monolayer graphene with its edge covered by PMMA. The central region of PMMA-covered graphene is opened (dark colored region in device) for selective doping. Inset shows an optical microscope image of a PMMA window-opened graphene device. The dashed line indicates the graphene edge. The Br_2 molecules are prohibited to intercalate between graphene layer and SiO_2.

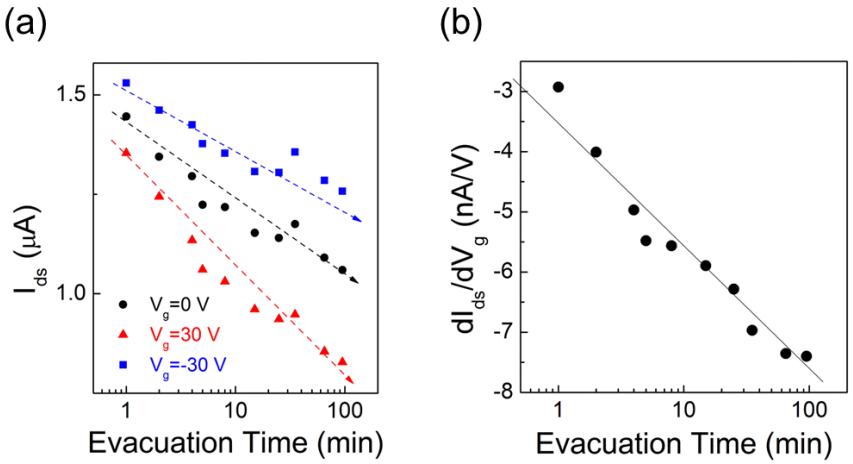

Figure 3.22. (a) Current flow as a function of evacuation time with various gate voltages in bi-layer graphene. (b) dI_{ds}/dV_g vs. evacuation time in bi-layer graphene

3.2 Summary

There are several halogen doping effect distinguished from other doping. First, *p*-type doping is exhibited in both mono and multi-layer graphene due to electron transfer from graphene to halogen species. Secondly, mobility reduction is found to be much weaker with halogen doping, compared to the case of other dopants [8-10]. Furthermore, the maximum resistance (R_{max}) of monolayer graphene at charge neutrality point is reduced, which is opposite to the increasing behavior of R_{max} upon doping with other dopants [8-10]. Such anomalous behaviors are not observed for monolayer graphene with its edge covered by a polymer layer. We attribute this anomalous halogen doping effect on monolayer graphene to the intercalation of halogen molecule between graphene and underlying SiO_2 substrate. By intercalating molecules, carrier scattering by the charged impurities embedded on SiO_2 is expected to be reduced, which compensate the additional scattering by introducing halogen molecules. These results demonstrate that halogen molecules can be an effective *p*-type dopants that enhance the conductivity of monolayer graphene without significant reduction of the carrier mobility. Moreover, when the graphene is doped, the residual carrier density is increased which contributes the carrier density increasing in electron-hole puddle. The doping induced residual carrier density is a crucial cause of R_{max} decreasing. In halogen-doped multi-layer graphene, hole doping is also observed. However, in contrast to monolayer, R_{max} increasing is measured with doping. Because halogen molecules can be intercalated into graphene layers and underlying graphene, we expect that screening effect can be weakened. However, intercalated effect is not found clearly, thus, further studies are needed.

Bibliography

[1] A. N. Rudenkoi, F. J. Keil, M. I. Katsnelson, and A. I. Lichtenstein, *Phys. Rev. B*, **82**, 035427 (2010)

[2] N. Y. Jung, N. D. Kim, S. Jockusch, N. J. Turro, P. Kim, and L. Brus, *Nano Lett*. **9**, 4133 (2009)

[3] G. Kalita, K. Wakita, M. Takahashi, and M. Umeno, *J. Mater. Chem*. **21**, 15209 (2011)

[4] N. Y. Jung, A. C. Crowther, N. D. Kim, P. Kim, L. Brus, *ACS Nano*, **4**, 7005 (2010)

[5] H. Wang, Y. Wu, C. Cong, J. Shang, and T. Yu, *ACS Nano*, **4**, 7221 (2010)

[6] Y. G. Lee, C. G. Kang, U. J. Jung, J. J. Kim, H. Jun Hwang, H. –J. Chung, S. Seo, R. Choi, and B. H. Lee, *Appl. Phys. Lett*. **98**, 183508 (2011)

[7] J. Martin, N. Akerman, G. Ulbricht, T. Lohmann, J. H. Smet, K. V. Klitzing, *Nature Phys*. **4**, 144 (2008)

[8] J. –H. Chen, C. Jang, S. Adam, M. S. Fuhrer, E. D. Williams, and M. Ishigami, *Nature Phys*. **4**, 377 (2008)

[9] K. Pi, K. M. McCreary, W. Bao, W. Han, Y. F. Chiang, Y. Li, S. –W. Tsai, C. N. Lau, and R. K. Kawakami, *Phys. Rev. B*, **80**, 075406 (2009)

[10] K. M. McCreary, K. Pi, A. G. Swartz, W. Han, W. Bao, C. N. Lau, F. Guinea, M. I. Katsnelson, and R. K. Kawakakmi, *Phys. Rev. B*, **81**, 115453 (2010)

[11] F. Chen, J. Xia, and N. Tao, *Nano Lett*. **9**, 1621 (2009)

[12] Y. –W. Tan, Y. Zhang, K. Bolotin, Y. Zao, S. Adam, E. H. Hwang, S. D. Sarma, H. L. Stormer, and P. Kim, *Phys. Rev. Lett*. **99**, 246803 (2007)
[13] X. Fan, L. Liiu, J. –L. Kao, and Z. Shen, *J. Phys. Chem*. **114**, 14939 (2010)

[14] C. Jang, S. Adam, J. –H. Chen, E. D. Williams, S. D. Sarma, and M. S. Fuhrer, *Phys. Rev. Lett*. **101**, 146805 (2008)

[15] J. –H. Chen, C. Jang, S. Xiao, M. Ishigami, and M. S. Fuhrer, *Nature Nanotech*, **3**, 206 (2008)

Chapter 4

Characterization by Raman Spectrum and AFM of Halogen-Doped Graphene

4.1 Results and Discussion

Here, we figure out the number of layers, doping effect, many electron effect and band gap opening by Raman spectrum. Additionally, we observed oxidation of graphene and metal electrode by halogen molecules by means of AFM.

Figure 4.2 shows an optical microscope image of Br_2-doped graphene layers on SiO_2 thickness of 300 nm. Layer 1 is monolayer and layer 2, 3 and 4 are multi-layers, which are distinguished by optical contrast. From the Raman spectrum, we expect to observe the doping effect. Black lines indicate the pristine graphene data and the colored lines (red, orange, green and blue) represent the doped data. The data are normalized with intensity of G-preak so as to compare the each amplitude of respective 2D-peaks. In Br_2-doped graphene, we also observed the doping effect from G-peak shift, 2D-peak reduction and G-peak splitting (Fig. 4.3). The G-peak splitting related to band gap opening is observed in multi-layer graphene, due to intercalation of Br_2 molecules into graphene layers. It is an agreement with that obtained as other reports [4]. Because of inhomogeneous distribution of intercalated Br_2 molecules, double degeneracy of G-peak is separated into two G-peaks.

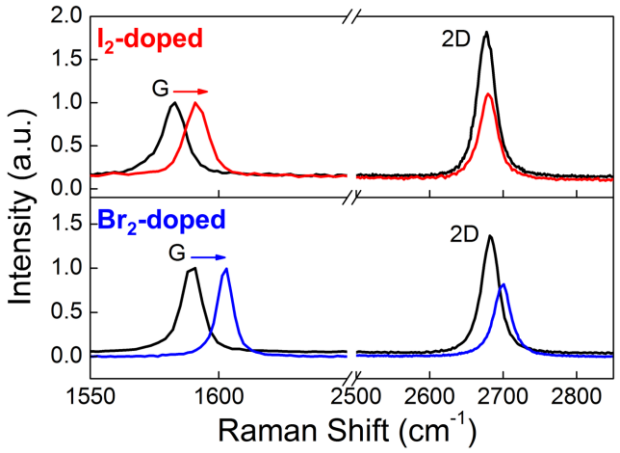

Figure 4.1. Raman spectrum of I_2- and Br_2-doped monolayer graphene. Black lines indicate the pristine graphene data and colored lines (red and blue) represent the spectrum of doped graphene. The data are normalized with G-peak intensity so as to compare the amplitude of respective 2D-peaks.

As the Br_2-doped graphene is aged in air, the intercalated Br_2 molecules can be desorbed. This behavior is shown in Fig. 4.4. These spectrums are obtained 2 months after Br_2-doping displayed in Fig. 4.3. The broad G-peaks (pink, yellow, light green and olive colored lines) are due to poor resolution of Raman spectrum compared with split data. Desorption of Br_2 molecules are found with red shift of G-peak in layer 1 and 2. On the contrary, in layer 3 and 4, thicker layers, the red shifts are not observed. It is considered that the intercalated Br_2 molecules are remained until 2 months. This can be a possibility of non-volatile memory device.

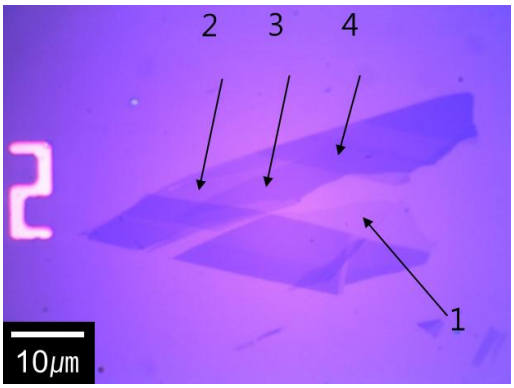

Figure 4.2. Optical microscope image of graphene layers doped with Br_2 (1 min) on SiO_2 thickness of 300 nm.

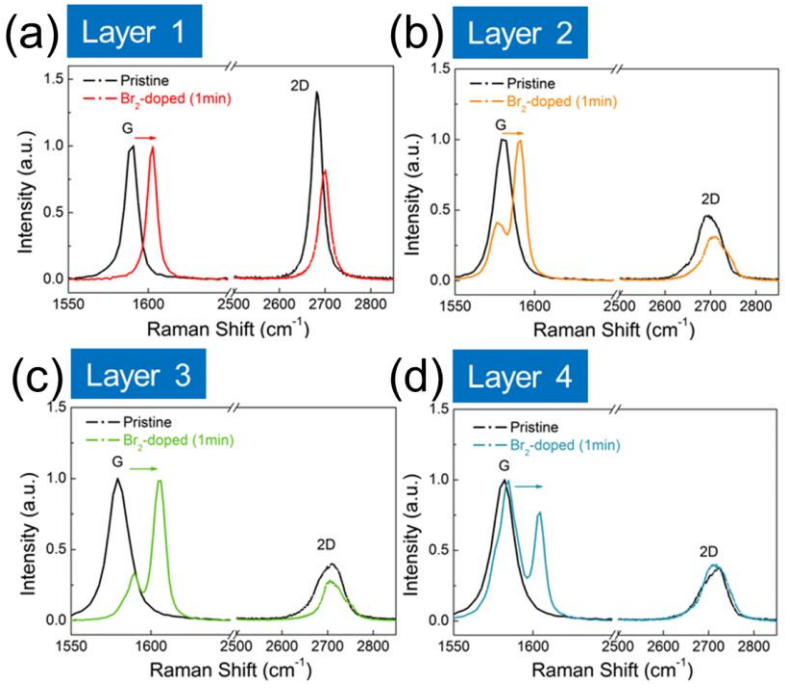

Figure 4.3. Raman spectrum of Br_2-doped graphene layers. (a), (b), (c) and (d) are the results of layer 1, 2, 3 and 4 in Fig. 4.2. Black lines indicate the pristine graphene data and colored lines (red, orange, green and blue) represent the spectrum of doped graphene.

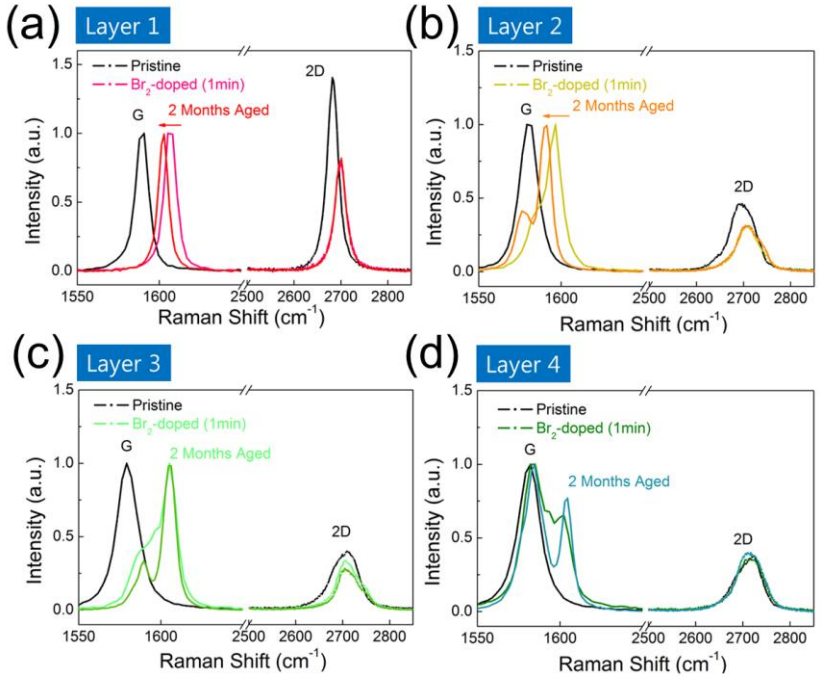

Figure 4.4. Raman spectrum of aged (2 months) graphene after Br_2 doping. (a), (b), (c) and (d) are spectrums of layer 1, 2, 3 and 4 in Fig. 4.2. As the time passed, the G-peaks tend to recover weakly in layer 1 and 2. However, in the thicker layers, layer 3 and 4, the recovery is not remarkable. It is expected that the intercalated Br_2 molecules in multi-layer graphene are not desorbed.

The surface of I_2-doped graphene is observed with AFM. We compare the morphology of graphene before and after doping, and different morphologies are obtained (Fig. 4.5). There are three distinguished results. First, the height of graphen is increased after doping from 1.6 nm to 2.7 nm (Fig. 4.5(b) and (d)). The height increasing is caused by adsorption of I_2 molecules upper and lower sides of graphene. It is roughly consistent with a distance between I2 intercalated HOPG layers (7.25 Å) [5]. Secondly, owing to adsorbed molecules, the roughness is increased. Lastly, damages by halogen molecules are shown at the side of metal electrodes, consisted to Ti and Au. Because the I_2 is highly oxidizing agent to metals, it seems to be attacked (Fig. 4.5(c) and 4.6 (a), (b)). This behavior is also shown in Br_2-doped device (Fig. 4.6 (b) and (c)). The electrodes are seems to be damaged irreversibly not only side but also top of the electrodes.

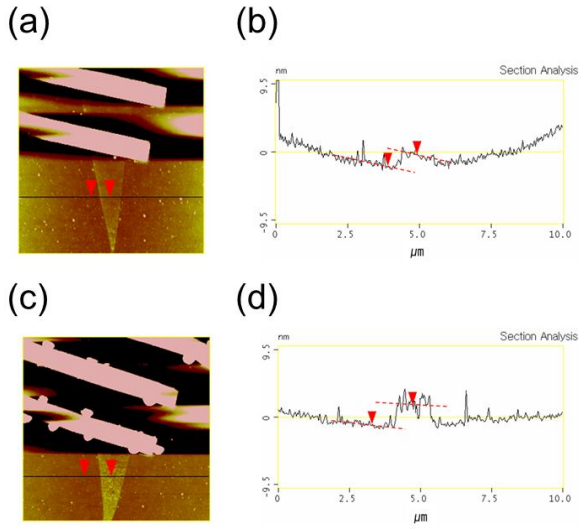

Figure 4.5. (a) An AFM image of undoped graphene. (b) The profile (height=1.6 nm) of undoped graphene. (c) An AFM image of I_2-doped graphene. (d) The height information (2.7 nm) of I_2-doped graphene. The height difference is caused by adsorption of I_2 molecules upper and lower side of graphene.

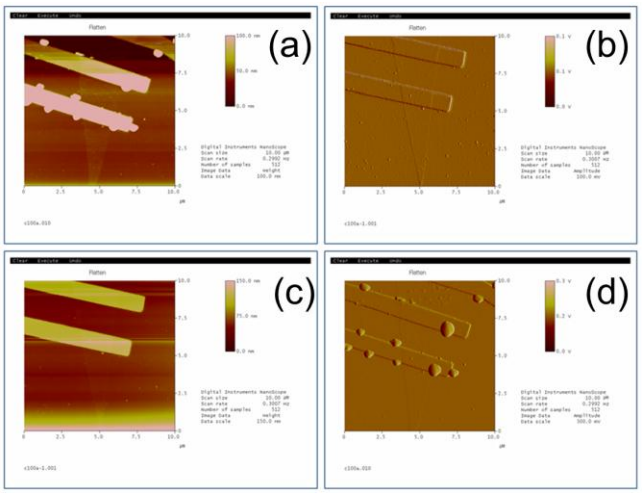

Figure 4.6. AFM images of a monolayer graphene device. (a) Height information and (b) voltage information of undoped graphene device. (c) Height information and (d) voltage information of I_2-doped graphene device. After doping, the height of graphene increases and some damages are generated around the edge of metal contacts by oxidation.

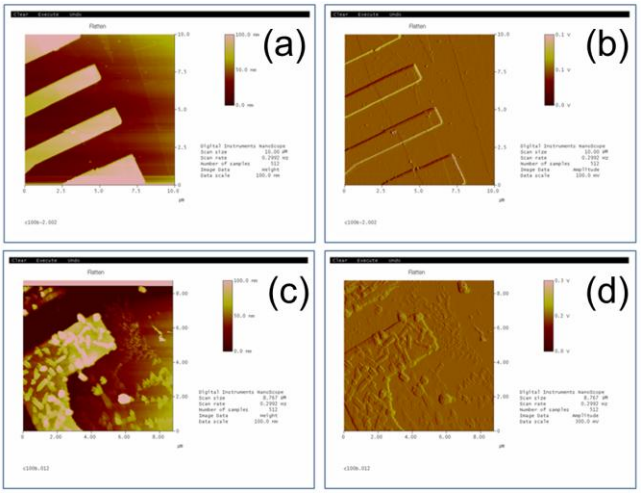

Figure 4.7. AFM images of a monolayer graphene device. (a) Height information and (b) voltage information of undoped graphene device. (c) Height information and (d) voltage information of Br_2-doped graphene device. After doping, a lot of defects are generated by oxidation. Because, Br_2 is a stronger oxidation material than I_2, the damages are shown at both the side and top of electrodes.

4.2 Summary

Raman spectrum of halogen-doped graphene on SiO_2 was obtained at room temperature in air. Three main doping effects in Raman spectrum are explained as below.

1. G-peak upshift : Removal of Kohn anomaly due to Fermi surface change by doping
2. FWHM reduction of G-peak : Fermi-level shift → Pauli exclusion → Decreasing of phonon decay into electron-hole pair
3. 2D-peak reduction : Electron density increasing → Electron-electron collision increasing → Number of DR processes decreasing

Additionally, the G-peak splitting was shown in Raman spectrum in Br_2-doped multi-layer graphene. Because of inhomogeneous position of intercalated Br_2 molecules in graphene layers, doubly degenerated G-peaks are split. These are typical characters of doped graphene. From above behaviors, we confirm the graphene doping again.

The surface images of I_2- and Br_2-doped graphene were observed with AFM. The height difference of I_2-doped monolayer graphene between before and after doping is ~1.1 nm. This is an evidence of molecular adsorption on graphene surface. It is expected that halogen molecules are adsorbed on both of upper and lower surfaces. It is roughly consistent with the layer distance of I_2-intercalated graphite (~7.25 Å). From the morphology of I_2- and Br_2-doped graphene and electrode, we found the several damages by oxidation with halogen molecules. The damages on metal electrode can be a barrier in electrical measurement of halogen-doped electronic structures.

Bibliography

[1] S. Pisana, M. Lazzeri, c. Casiraghi, K. S. Novoselov, A. K. Geim, A. C. Ferrari, and F. Mauri, *Nature Mater*. **6**, 198 (2007)

[2] J. Yan, Y. Zhang, P. Kim, and A. Pinczuk, *Phys. Rev. Lett*, **98**, 166802 (2007)

[3] D. M. Basko, S. Piscanec, and A. C. Ferrari, *Phys. Rev. B*, **80**, 165413 (2009)

[4] N. Y. Jung, N. D. Kim, S. Jockusch, N. J. Turro, P. Kim, and L. Brus, *Nano Lett*. **9**, 4133 (2009)

[5] C. –C. Hung, an D. Kucera, *Carbon*, **32**, 1441 (1994)

Chapter 5

Conclusion

We report electron scattering effect on halogen-doped mono and multi-layer graphene by measuring of electrical transport at room temperature. The doping effect is also confirmed with Raman spectrum.

First, we discuss the electron scattering effect on I_2- and Br_2-doped monolayer graphene. The gate-dependent linear conductivity of graphene on SiO_2 is considered as an evidence of charged impurity scattering. In halogen-doped graphene, the linear behavior was also observed with additional effects. The charge neutrality point (CNP) is shifted to hole carrier regime, a cause of *p*-doping by halogen molecules. The measured mobility and maximum resistance at CNP give crucial point for understanding of carrier scattering in graphene. Charged impurity scattering considered as the most important interaction in doped graphene. In halogen doping, the doping-induced impurities are another scattering source. Because of these scatterings, graphene mobility is limited. The difference between halogen doping-induced scattering and charged impurity scattering is studied with the comparison of mobility and R_{max} by other dopants. In case of halogen doping, mobility reduction is small compared to other doping. The ratio of CNP shift and inverse of mobility in halogen doping is relatively large, b=17.8 and 11.8 for electron and hole mobility, respectively. This implies the small reduction of mobility with doping, which is interpreted as screening of scattering with charged impurities on SiO_2. It is an advantage of halogen doping for high mobility and high conductivity graphene device. Moreover, R_{max} decreasing with doping is a distinguished property from other types of doping. In K, Ti,

Au, Fe and Pt doping, R_{max} was increased or nearly constant with doping. This is understood with increasing of doping-induced residual carrier density. When halogen dopants are adsorbed on graphene, the charge carrier density is increased in inhomogeneous potential fluctuation, electron-hole puddle. Even though small reduction of mobility, residual carrier density increasing is a cause of resistance decreasing at CNP. By means of doping with PMMA window-opened graphene, we confirmed that R_{max} decreasing is a result of an effect by screening of the scattering of charged impurities underlying graphene layer.

Second, in multi-layer graphene, similar doping effects are observed except R_{max} change. Halogen molecules can be intercalated into graphene layer as well as adsorbed on graphene surface. Therefore, we expect that residual carrier density is less affected than doping in monolayer graphene. However, unfortunately, it we do not fully understand the reason of residual carrier density change in multi-layer graphene. In order to interpret the R_{max} in multi-layer graphene, further studies are needed.

Third, we confirmed the doping effect with Raman spectroscopy. G-peak shift shows the Kohn anomaly removal due to Fermi-level shift at K-point. The FWHM decreasing is also an evidence of doping. And high carrier density by doping causes electron-electron interaction, which is a result of 2D-peak reduction. In Br_2-doped multi-layer graphene, G-peak splitting is measured because of degeneracy breaking (G-peak) due to inhomogeneous distribution of halogen molecules in graphene layers. It shows a possibility of band gap opening in Br_2-doped graphene. On the contrary, I_2-doped graphene, the splitting was not observed. It is interpreted with the relative larger molecular size of I_2.

Finally, halogen adsorption on monolayer graphene is observed with AFM. From AFM profile, we compare the height between doped- and undoped-graphene. As a result, the height difference is ~7.25 Å which is roughly consistent with a distance of I_2-intercalated graphite layers. Additionally, we observed the morphology of oxidized graphene and metal electrodes. In both of I_2 and Br_2 doping, several damages are shown. This oxidation can be an obstacle of halogen doping on electronic device fabricated with metal structures.

국문초록

이 학위논문에서는 할로겐 분자(요오드, 브롬) 를 이용하여 화학적으로 도핑된 그래핀의 전하수송특성에 관한 연구에 대한 내용을 작성하였다. 도핑에 대한 증거는 또한 라만 스펙트럼으로 확인하였다. 여기에서 우리는 도핑된 그래핀의 전하수송 특성이 도핑 첨가물에 의한 산란현상을 탐구하는 기회를 제공할 것으로 기대한다.

우리는 할로겐 물질인 요오드와 브롬 분자를 이용하여 단 겹, 여러 겹 그래핀의 전하수송 현상을 연구하였다. 단 겹 그래핀에서 이 도핑의 경우, p 타입 도핑을 의미하는 전하 중성 점의 홀 영역 이동, 그리고 전하 이동도의 감소를 관찰하였다. 그러나, 다른 물질을 이용한 도핑의 경우와 비교했을 때, 할로겐 도핑에 의한 전하이동도 감소는 매우 약하다. 이에 할로겐 분자는 전하 이동도를 심하게 저하시키지 않는 동시에 전하밀도를 변화시킬 수 있는 효과적인 도핑 첨가물이라 할 수 있다. 이는 그래핀과 실리콘 옥사이드 사이에 삽입된 할로겐 분자에 의한 스크린 효과 때문에 전하 불순물 산란이 감소되었기 때문으로 이해된다. 또한 전하 중성 점에서 저항의 최대값이 연속되는 도핑에 따라 감소하는데, 이는 칼륨, 티타늄, 백금, 철, 금 과 같은 도핑 첨가물과 다른 특성이다. 이는 단 겹 그래핀의 경우 할로겐 도핑의 고유한 특성이다. 또한 전하 이동도와 저항의 최대값을 다른 도핑 결과와 비교하였다. 저항의 최대값은 할로겐 도핑에 의해 그래핀 표면에 형성된 불순물과 실리콘 옥사이드에 존재하는 불순물에 의해 형성된 전자-홀 웅덩이가 만들어 낸 잔여 전하밀도와 연관되어 있다. 할로겐 분자는 그래핀 표면의 전자-홀 웅덩이에 전하를 주입하는 역할을 한다. 따라서 도핑에 의한 잔여 전하밀도 증가는 전하 중성 점에서 그래핀의 전기전도도 증가에 기여한다. 이 결과를 확신하기 위해 그래핀의 가장자리를 고분자 층으로

덮고 선택적으로 도핑 하였다. 그 결과 앞서 관찰한 특이한 현상들이 더 이상 나타나지 않았다. 따라서, 이 실험 결과들은 그래핀과 실리콘 옥사이드 사이에 삽입된 할로겐 분자들이 실리콘 기판에 존재하는 전하 불순물을 스크린 한 결과로 이해할 수 있다.

여러 겹 그래핀에서 홀 도핑은 전하 중성 점의 이동으로 관찰되었다. 그러나, 단 겹 그래핀의 경우와 달리, 저항의 최대값은 도핑에 따라 증가하였다. 할로겐 분자들이 그래핀-그래핀 사이와 그래핀 층들의 하단에 삽입되었기 때문에 스크린 효과가 약해 질 수 있다. 하지만, 불행하게도 이 효과에 대한 분명한 원인은 밝혀지지 않았다. 이 효과를 이해하기 위해서는 정성적이고 정량적 분석이 더 이루어져야 할 것으로 생각한다.

도핑 효과는 전하수송 측정 뿐 아니라 라만 스펙트럼을 통해서도 관측되었다. 비록 도핑 된 그래핀에 대한 여러 라만 결과들이 선행되었다고 할 지라도, 이는 할로겐 도핑에 대한 유용한 정보를 제공한다. 할로겐 도핑에 대한 두 가지 주된 효과는 다른 물질을 이용한 도핑에서도 잘 알려져 있다. 첫 번째는 요오드와 브롬 도핑 된 단 겹 그래핀에서 양의 방향으로의 G-밴드 이동이다. 특이하게도, 브롬 도핑 된 여러 겹 그래핀에서 G-밴드 갈라짐이 관측되었는데, 이는 그래핀 층 사이로 브롬 분자가 삽입된 결과이다. 두 번째로, 2D-밴드 크기의 감소이다. 이는 전자 간 산란 효과로서 이해되고 있다. 추가적으로 할로겐 도핑의 안정성을 G-밴드 이동으로 가늠하였다. 도핑 두 달 결과 후 G-밴드의 음의 방향 이동이 관측되었다. 그러나 겹 수가 증가함에 따라 그 이동은 작거나 무시 할 만한 수준이다.

이 실험은 전기 신호 측정을 위한 전극의 산화를 최소화 하기 위해 고 진공에서 수행되었다. 그리고 할로겐 도핑은 상온에서 할로겐 분자에 반응성이 없는 유리 튜브 내에서 이루어 졌다.

주요어 : 그래핀, 할로겐 도핑, 전하수송, 전하 불순물 산란, 도핑에 의해 유도된 불순물 산란, 라만 스펙트럼

학번 : 2002-30142

감사의 글

무더운 여름입니다. 밖으로 나가면 땀이 옷 사이로 줄줄 흘러 내립니다. 많은 분들이 뜨거운 체온을 밖으로 흘려 보내고 계시겠지요. 반면에 저는 시원한 에어컨 바람을 맞으며 글을 적습니다. 편한 의자에 앉아 모니터를 바라봅니다. 다른 분들의 체온에 의한 혜택입니다. 제가 처한 환경과, 저가 해야 하는 일의 성격 때문에 기본적으로 누려야 하는 '감사' 라고 하기엔 많이 사치스럽습니다. 위를 향한, 수평 한 시선일 때는 바라보기 어려운, 한 번 생각하고 지나가기 바쁜 마음이기에 항상 마음 한 켠에 빚이 있습니다.

제가 작성한, 비록 미숙한 논문이지만, 이 결과물이 출간되기까지 도움을 주신 모든 분들께 진심으로 감사 드리며, 말로 다 전할 수 없음을 송구하게 생각합니다. 이 결과물은 결코 저 혼자서 작성할 수 있는 결과물이 아니며, 여러 분 들의 도움으로 작성되었음을 알고 있습니다. 연구 주제의 큰 틀을 정해주시고, 어려운 순간에 항상 힘이 되어 주신 지도교수님께 감사 드립니다. 자상한 격려보다 미숙할 때의 꾸짖음이 더 정겨움을 마지막에서야 느껴봅니다. 이 연구주제를 긍정적으로 바라봐 주시고 지도해 주신 논문 지도교수님들께 감사 드립니다. 또한 부족한 후배의 길을 어떻게든 터주려 애써주신 동철 형, 준성 형, 상욱이 형, 병훈이 형, 정호 형께 감사 드립니다. 갓 복학한 게으른 후배에게 새로운 연구로의 길을 보여주신 재승 형, 언제나 부족한 후배의 투정 받아주신 동수형, 먼저 졸업해서 뒷사람의 이정표가 되어주는 세정, 승주, 아정, 영수 에게도 애정 어린 감사를 전합니다. 외에도 1년 남짓 연구활동을 도와주시고 격려해 주신 서순애 교수님, 정현종 박사님, 우윤성 박사님께도 감사 드립니다.

선배로써 든든한 디딤돌이 되어주지 못한 실험실 후배들에게 미

안한 마음입니다. 스웨덴에서 다른 이들을 대신해 시간을 책임지고 있는 영우, 항상 저의 앞을 터주고, 뒤를 챙겨 주던 승재, M자형 탈모와 1년 연장의 날벼락에도 불구하고 펜실베니아에서 밝은 모습 잃지 않는 성주, 허술하고 허술하며 허술하고 허술하니 모든 것이 허술한 경호, 까탈스럽고 2% 부족하지만 실험실의 든든한 기둥이 된 민, 모두가 자기 위치에서 빛을 낼 사람들이고, 곧 좋은 짝 들 만날 것으로 기대하고 있습니다. 그리고 무한 스트레스를 온몸으로 받아내며 용케 견디고 있는 지현씨에게도 안쓰러움과 감사의 마음을 전합니다. 물리학의 기초를 다듬어 주고 변치 않을 우정을 보여주신 물리공간 선 후배님 들께도 감사의 마음을 전합니다.

변치 않는 사랑으로 부족하기 짝이 없는 아들 지켜봐 주시는 아버지, 어머니께 감사 드리며. 끝으로, 졸업하기 까지 오랜 시간 참고 기다려 준 아내와 희재에게 감사의 마음을 전합니다.

2012. 7. 23

22동 216호 에서 추승완